BIOLOGICAL SCIENCES – Microbiology

A lipocalin mediates unidirectional haem biomineralization in malaria parasites

Joachim M. Matz[1,2,*], Benjamin Drepper[2], Thorsten B. Blum[3], Eric van Genderen[3], Alana Burrell[4], Peer Martin[2], Thomas Stach[2], Lucy Collinson[4], Jan Pieter Abrahams[3,5,6], Kai Matuschewski[2] & Michael J. Blackman[1,7]

[1] Malaria Biochemistry Laboratory, The Francis Crick Institute, London, UK
[2] Department of Molecular Parasitology, Institute of Biology, Humboldt University, Berlin, Germany
[3] Laboratory of Nanoscale Biology, Division of Biology and Chemistry, Paul Scherrer Institute, Villigen, Switzerland
[4] Electron Microscopy Science Technology Platform, The Francis Crick Institute, London, UK
[5] Center for Cellular Imaging and NanoAnalytics, Biozentrum, University of Basel, Basel, Switzerland.
[6] Institute of Biology, Leiden University, Leiden, The Netherlands.
[7] Faculty of Infectious and Tropical Diseases, London School of Hygiene & Tropical Medicine, London, UK
* Corresponding author: J.M.M., joachim.matz@crick.ac.uk, https://orcid.org/0000-0002-0575-0412

ABSTRACT

During blood stage development, malaria parasites are challenged with the detoxification of enormous amounts of haem released during the proteolytic catabolism of erythrocytic haemoglobin. They tackle this problem by sequestering haem into bioinert crystals known as haemozoin. The mechanisms underlying this biomineralization process remain enigmatic. Here, we demonstrate that both rodent and human malaria parasite species secrete and internalize a lipocalin-like protein, PV5, to control haem crystallization. Transcriptional deregulation of *PV5* in the rodent parasite *Plasmodium berghei* results in inordinate elongation of haemozoin crystals, while conditional *PV5* inactivation in the human malaria agent *Plasmodium falciparum* causes excessive multi-dimensional crystal branching. Electron diffraction analysis indicates that neither the crystalline order nor unit cell of haemozoin are affected by impaired PV5 function. Deregulation of PV5 expression renders *P. berghei* hypersensitive to the antimalarial drugs artesunate, chloroquine, and atovaquone, resulting in accelerated parasite clearance following drug treatment *in vivo*. Together, our findings demonstrate the *Plasmodium*-tailored role of a lipocalin family member in haemozoin formation and underscore the haem biomineralization pathway as an attractive target for therapeutic exploitation.

KEYWORDS

Plasmodium, malaria, haemozoin, vacuole, lipocalin

SIGNIFICANCE

During blood stage development, the malaria parasite replicates inside erythrocytes of the vertebrate host, where it engulfs and digests most of the available haemoglobin. This results in release of the oxygen-binding prosthetic group haem, which is highly toxic in its unbound form. The parasite crystallizes the haem into an insoluble pigment called haemozoin, a process that is vital for parasite survival and which is exploited in antimalarial therapy. We demonstrate that the parasite uses a protein called PV5 in haemozoin formation and that interfering with PV5 expression increases the parasite's sensitivity to antimalarial drugs during blood infection. An improved understanding of the mechanism underlying haem sequestration will provide valuable insights for future drug development efforts.

INTRODUCTION

The devastating pathology of malaria is caused by infection of red blood cells with unicellular *Plasmodium* parasites which reside within an intraerythrocytic parasitophorous vacuole (PV) (1). Throughout blood stage development, the parasite ingests up to 80% of the host cell cytoplasm, facilitating amino acid acquisition and making sufficient room for parasite growth (2, 3). Haemoglobin breakdown is carried out by an array of functionally redundant proteases and occurs in acidified lysosome-like organelles with species-specific morphology (4). In the rodent-infective parasite species *Plasmodium berghei*, one or more haemoglobin-containing food vacuoles (FV) give rise to small digestive vesicles (DVs) where active haemoglobin catabolism occurs and which only fuse at the very end of intraerythrocytic development (5). By contrast, the most virulent agent of human malaria, *Plasmodium falciparum*, directs all endosomal traffic to a single large FV, where proteolysis occurs. The DVs of *P. berghei* and the FV of *P. falciparum* are therefore functionally equivalent (6).

Here, haemoglobin digestion is accompanied by the release from the globin chains of high levels of the porphyrin co-factor haem, which can damage proteins and lipids through various mechanisms, including the formation of free radicals (7). The unique challenge of haem detoxification is met by the parasite's capacity to sequester the released haem into a bioinert crystalline product called haemozoin (Hz), which accumulates in the FV or DVs. Haem is initially oxidised to yield haematin, which then dimerizes through the reciprocal coordination of iron and propionate moieties. This molecular unit then assembles into crystals which typically take the form of triclinic high aspect ratio parallelograms (8-10). By the end of intraerythrocytic development, all the Hz crystals are contained within a central residual body, which is eventually released upon parasite egress from the host cell and which contributes to the inflammatory responses associated with acute malaria (11). The mechanism of Hz formation is highly debated. While several studies suggest a conventional physicochemical and autocatalytic crystallization mechanism (12-15), there have been reports of parasite proteins (16-18) and lipids (19-21) promoting Hz assembly *in vitro*.

The parasite's dependency on haem detoxification has long been exploited in antimalarial therapy with outstanding success. Aminoquinolines inhibit Hz formation *via* direct physical interactions with haematin and the crystal surface, eventually leading to the build-up of cytotoxic free haem (22-25). The aminoquinoline chloroquine was the front-line medication against malaria from the 1950s onward until the emergence of wide-spread drug resistance restricted its utility (26). Nonetheless, to this day, chloroquine remains among the most effective antimalarial drugs ever developed, highlighting the outstanding importance of haem

81 sequestration for *Plasmodium* survival. It is thus crucial for future drug development efforts to
82 gain a better understanding of the mechanisms underlying this unique biomineralization event.

83 In this report, we demonstrate that a parasite lipocalin-like protein called PV5 is a
84 central regulator of *Hz* formation.

85 **RESULTS**

86 **Malaria parasites encode a lipocalin-like protein, PV5**

87 Employing a genome-wide *in silico* down-scaling approach, we previously identified an
88 essential *P. berghei* PV protein, *Pb*PV5, which has orthologues in all other *Plasmodium*
89 species (27). Inspection of the PV5 amino acid sequence revealed a striking similarity to
90 members of the functionally diverse lipocalin family, barrel-shaped proteins capable of binding
91 various hydrophobic ligands and/or protein interaction partners (28). The signature lipocalin
92 fold comprises a short amino-terminal helix followed by eight consecutive barrel-forming β-
93 strands, another α-helix and one more β-strand (Fig. 1*A*) (29). In addition, PV5 harbours two
94 preceding amino-terminal β-strands specific to *Plasmodium*, as well as a signal peptide.
95 Multiple sequence alignments with lipocalins from phylogenetically distant organisms showed
96 the presence of a highly conserved glycine and two aromatic amino acids within the
97 structurally conserved region 1 (SCR1) of PV5, a hallmark of the extended calycin superfamily
98 (Fig. 1*A*) (29). Among several structural homologues, the bacterial outer membrane lipocalin
99 Blc from *Escherichia coli* was predicted to share the highest similarity with PV5. Blc-guided
100 structure homology modelling suggests that PV5 shares the overall architecture of the lipocalin
101 family including the characteristic β-barrel (Fig. 1*B*). Together, the sequence signatures and
102 predicted structural features support membership of *Plasmodium* PV5 in the calycin protein
103 superfamily.

104 **PV5 localizes to the PV and DVs in *P. berghei***

105 We first investigated the spatiotemporal expression of *Pb*PV5 during asexual blood stage
106 development. Live fluorescence microscopy of transgenic *P. berghei* parasites expressing
107 mCherry-3xMyc-tagged *Pb*PV5 confirmed that *Pb*PV5 localizes to tubular PV extensions
108 during ring and trophozoite stages and surrounds individual merozoites in segmented
109 schizonts (Fig. 1*C*) (27). In addition, a substantial fraction of the protein was restricted to the
110 parasite cytoplasm. This was particularly prominent in schizonts, where intraparasitic *Pb*PV5
111 appeared to localize to the Hz-containing residual body (Fig. 1*C*). In merozoites, mCherry
112 fluorescence was concentrated in a punctate intraparasitic region, perhaps signifying storage
113 of *Pb*PV5 in the dense granules, as has been demonstrated for several other important PV
114 proteins (30-32), but this fraction was minimal as compared to the protein contained in the
115 residual body. Quantification of the mCherry-fluorescence intensity in live parasites indicated
116 that *Pb*PV5 is much more abundant in mature parasite stages than in rings and merozoites,
117 suggesting substantial levels of *de novo* synthesis throughout parasite maturation (Fig 1*C*).

118 In trophozoites, the intraparasitic fraction of *Pb*PV5 was associated with spherical
119 structures at the parasite periphery (Fig. 1*C*) and microscopic examination of mechanically
120 expanded free parasites revealed that these were the Hz-containing DVs (Fig. 1*D)*. Here,
121 *Pb*PV5 was freely soluble, as indicated by subcellular parasite fractionation (Fig. 1*E*).
122 Together, our observations suggest that *Pb*PV5 is a calycin family member that is first
123 secreted into the PV and then internalized during endocytosis of host cell cytoplasm to
124 accumulate in the matrix of the DVs.

125 **Transcriptional deregulation of Pb*PV5* impairs asexual parasite propagation *in vivo***

126 Our previous attempts to disrupt the genomic Pb*PV5* locus resulted only in atypical integration
127 of the targeting construct without perturbing the endogenous gene, which is indicative of
128 essential functions during the asexual blood stage cycle *in vivo* (27). As an alternative genetic
129 strategy to analyse Pb*PV5* function, we sought to deregulate Pb*PV5* expression by employing
130 a promoter swap approach (Fig. 2*A*). We thus generated parasites expressing the
131 endogenous Pb*PV5* gene from the promoters of *Plasmodium* translocon of exported proteins
132 88 (*PTEX88*) or heat shock protein 101 (*HSP101*), respectively (*SI Appendix*, Fig. S1 *A* and
133 *B*). Previously published RNA sequencing data predicted that expression under these
134 heterologous promoters would result in considerable downregulation to 2–20% of WT Pb*PV5*
135 steady state transcript levels, respectively, depending on the developmental stage (33).
136 However, quantitative real-time PCR analysis of the mutants indicated that the knock-down
137 efficiency was only ~60% in asynchronous blood stages (*SI Appendix*, Fig. S1*C*). These
138 differences did not reach statistical significance, likely due to variation in the composition of
139 the mixed blood stages. By contrast, mutant schizonts exhibited significantly elevated Pb*PV5*
140 transcript levels, corresponding to ~3.4 (*pv5::5'ptex88*) and ~5.6 times (*pv5::5'hsp101*) more
141 than in WT schizonts (*SI Appendix*, Fig. S1*C*). These unexpected dynamics might be
142 explained by compensatory mechanisms and/or locus-dependent promoter activities.
143 Importantly, using the promoter swap strategy, we succeeded in deregulating the physiological
144 expression of Pb*PV5*.

145 To investigate whether altered Pb*PV5* transcription results in reduced parasite fitness,
146 we examined asexual propagation of the mutants *in vivo*. Growth of the promoter swap
147 mutants was significantly impaired, with the *pv5::5'ptex88* parasites growing at 80% and
148 *pv5::5'hsp101* parasites at only 54% of the WT growth rate (Fig. 2*B*). These results underline
149 the importance of correct Pb*PV5* expression during asexual replication of the parasite *in vivo*
150 (Fig. 2*B*).

151 **Pb*PV5* mutants form less Hz**

152 Inspection of Giemsa-stained thin blood films revealed striking morphological differences
153 between WT parasites and the promoter swap mutants. During the trophozoite stage, the FV
154 of the mutants was significantly swollen, visible as a translucent area within the parasite
155 cytoplasm close to the nucleus (Fig. 2*C*). Microscopic quantification revealed this area to be
156 1.5-fold (*pv5::5'ptex88*) or 1.8-fold (*pv5::5'hsp101*) larger than in WT parasites (*SI Appendix*,
157 Fig. S2*A*). Vacuolar swelling was transient, as mature schizonts did not exhibit comparable
158 abnormalities (Fig. 2*C*).

159 Another striking phenomenon was the low visibility of dark granular material in mutant
160 trophozoites, when compared to WT (Fig. 2*C*). This was most noticeable in the *pv5::5'hsp101*
161 mutant and became particularly apparent during the gametocyte stage, where pigment
162 granules are usually very prominent. To validate the visually observed lack of granularity, we
163 subjected mixed blood stage parasites to flow cytometry and measured the intensity of the
164 side scattered light, a commonly used proxy for cellular granularity (*SI Appendix*, Fig. S2*B*).
165 In agreement with our microscopic analysis, the Pb*PV5* mutants displayed reduced side
166 scattering and the phenotype was again more severe in the *pv5::5'hsp101* mutant.

167 Because we suspected a Hz formation defect in the mutants, we fixed intraerythrocytic
168 parasites with methanol and subjected them to reflection contrast polarized light microscopy,
169 which exploits the birefringent properties of Hz to specifically visualize the crystals. Using this
170 method, we detected a weaker signal for the mutants, which correlated with reduced visibility
171 of dark pigment in brightfield (Fig. 2*D*). Enumeration of individual bright entities suggested the
172 presence of fewer Hz-containing structures within the mutants (~80% of WT) (Fig. 2*D*).
173 Quantification of the reflected polarized light intensity also indicated that *pv5::5'ptex88*
174 parasites form only 64% and the *pv5::5'hsp101* 61% of the Hz generated in WT parasites (*SI*
175 *Appendix*, Fig. S2*C*). Together, these observations show that perturbation of Pb*PV5*
176 expression results in reduced haem biomineralization *in vivo*.

177 **Protracted Hz extension upon deregulation of Pb*PV5* expression**

178 We next aimed to examine how lower levels of Hz correlate with crystal size. To do this we
179 isolated Hz from mixed blood stage parasites and examined the material by scanning electron
180 microscopy (SEM). This confirmed the characteristic high aspect ratio parallelogram
181 morphology of WT Hz (Fig. 2 *E* and *F*). Strikingly, this was not the case for crystals isolated
182 from the promoter swap mutants. Hz from both transgenic parasite strains exhibited highly
183 irregular shapes and rough edges and showed only few of the distinctive Hz crystal vertices
184 (Fig. 2*F*). Crystals from *pv5::5'ptex88* parasites most often had a pointed and canine tooth-

185 like appearance, extending from a single straight crystal face. These abnormalities were even
186 more pronounced in the *pv5::5'hsp101* mutant, where in most cases there was a region of
187 normal crystal morphology with 2 or 3 straight edges, corresponding to the {010}, {011} and
188 {001} faces. From this regular parent crystal emerged an enormous outgrowth which usually
189 surpassed the dimensions of the parent crystal (Fig. 2*F*). This outgrowth consistently grew at
190 an obtuse angle of ~105° in relation to the dominant *c* axis of the parent crystal, although
191 accurate determination of the angle was complicated by the slightly bent and irregular shape
192 of the outgrowth, which might be attributed to the space restrictions encountered in the *P.*
193 *berghei* DVs. The outgrowth's angle was not reflected in the physiological morphology of Hz
194 (Fig. 2 *E* and *F*) and at least two faces of the regular parent crystal appeared to be involved.
195 Indeed, in most cases, the outgrowth emerged from sites where the {010} and {011} faces
196 meet and always grew along a plane corresponding to one of the original crystal faces (Fig.
197 2*F*). Other crystal formations were also observed, albeit at lower frequency, including some
198 with multiple crystal branches and some with very rough surfaces (*SI Appendix*, Fig. S2*D*).
199 We observed similar crystal abnormalities *in situ* by transmission electron microscopy (TEM)
200 of purified schizonts (Fig. 2*G*).

201 Despite the lower overall levels of Hz formed and the abnormal crystal morphology,
202 we found that the mutants formed larger Hz crystals as indicated by the area exposed to the
203 SEM electron beam (Fig. 2*H*). The *pv5::5'hsp101* mutant formed the largest crystals, which
204 were ~177% of WT size, while the *pv5::5'ptex88* crystals were at 130%. Importantly, the
205 mutant Hz crystals displayed greater dimensions only in length but not in width owing to the
206 unidirectional expansion of the outgrowth (Fig. 2*H*). Examination of the parent crystals from
207 *pv5::5'hsp101* parasites showed that these were roughly half the size of whole WT crystals
208 (Fig. 2*H*). The aspect ratios of WT crystals and the *pv5::5'hsp101* parent crystals were
209 identical, together indicating that a period of normal crystallisation during earlier *pv5::5'hsp101*
210 parasite development is followed by irregular crystal extension later on (*SI Appendix*, Fig.
211 S2*E*). Inspection of Hz from an unrelated slow-growing mutant (34) and from chloroquine-
212 treated WT parasites ruled out a secondary effect of reduced parasite fitness or mortality on
213 Hz morphology (*SI Appendix*, Fig. S2 *F* and *G*).

214 To determine whether the crystalline order was affected by deregulation of Pb*PV5*, we
215 obtained electron diffraction patterns from WT- and *pv5::5'hsp101*-derived Hz (Fig. 2*I*) and
216 analysed the maximum diffracted intensities in concentric bins as a function of resolution.
217 There was no difference in the drop-off of diffracted intensity between WT and mutant and the
218 peak positions of the maxima corresponded (Fig. 2*J*). Differences in the magnitude of
219 individual peaks can be attributed to preferential orientation, especially of the *pv5::5'hsp101*-
220 derived crystals, which most often come to lie at their {100} faces. Together, these data

221 indicate no differences in crystalline order or unit cell upon functional impairment of *PbPV5*
222 and we conclude that altered crystal morphology is not caused by alternative nucleation into
223 a different haematin polymorph. Thus, deregulation of Pb*PV5* leads to the formation of ordered
224 elongated Hz crystals with a highly variable and abnormal habit.

225 **PV5 controls Hz branching in *P. falciparum***

226 To investigate the consequences of *PV5* disruption, we generated a conditional *PV5* knockout
227 line of the human pathogen *P. falciparum*, allowing rapamycin-induced DiCre-mediated
228 excision of the Pf*PV5* gene (Fig. 3*A* and *SI Appendix*, Fig. S3*A*). Correct modification of the
229 locus was indicated by diagnostic PCR and by the successful tagging of *Pf*PV5 with a 3xHA
230 tag, as demonstrated by Western blot and immunofluorescence analysis (Fig. 3 *C* and *D* and
231 *SI Appendix*, Fig. S3 *B* and *C*). As in *P. berghei*, tagged PV5 localized to the PV and to
232 intraparasitic vesicular structures in *P. falciparum*. No signal was observed within the central
233 FV (*SI Appendix*, Fig. S3*C*).

234 Treatment of *pv5-3xHA:loxP* parasites with rapamycin led to efficient gene excision
235 and complete loss of *Pf*PV5 protein expression during the same intraerythrocytic cycle (Fig. 3
236 *B-D*). This did not detectably affect parasite maturation but did result in a modest merozoite
237 invasion defect upon rupture of the Pf*PV5*-null schizonts, reducing parasite replication (*SI*
238 *Appendix*, Fig. S4 *A-C*). Extended monitoring of the rapamycin-treated parasites showed that
239 despite this ~40% fitness cost, Pf*PV5* appeared to be dispensable for asexual blood stage
240 growth *in vitro* (*SI Appendix*, Fig. S4*B*).

241 To examine the effects of Pf*PV5* ablation on haem biomineralization, Hz released at
242 parasite egress was examined by light microscopy of fixed Giemsa-stained culture smears.
243 This revealed that in the absence of *Pf*PV5 Hz no longer formed clusters of separate elongated
244 crystals, but rather appeared as aggregates which only occasionally fell apart into individual
245 globular units (Fig. 3*E*). Accordingly, microscopic inspection of live parasites revealed that the
246 characteristic twirling motion of Hz within the central FV was largely lost upon Pf*PV5* knockout
247 (Fig. 3*F* and *SI Appendix*, Movie S1).

248 The dramatic abnormalities in *Hz* crystal morphology resulting from ablation of Pf*PV5*
249 were even more evident by SEM analysis. While WT parasites formed crystals of the expected
250 brick-like morphology, individual Hz units from rapamycin-treated *pv5-3xHA:loxP* parasites
251 appeared smaller and more globular (Fig. 3*G* and *SI Appendix*, Table S1). The surfaces of
252 these Hz units were covered in scales and stubby crystal buds. Individual crystals of
253 comparable bud-like dimensions were not observed, indicating a branching rather than an
254 aggregation phenomenon. In some instances, a lower number of crystal buds allowed the

255 visualization of an ordered Hz core, suggesting that branching is initiated from a regular parent
256 crystal (Fig. 3*G*). We observed several morphological intermediates between slightly scaled
257 Hz, highly branched crystal units and fused congregations (Fig. 3*G*). We frequently observed
258 enormous aggregates of spherical proportions, mirroring the shape of the central FV (Fig. 3*G*).
259 This suggested that hyperactive crystal branching in the absence of *Pf*PV5 caused individual
260 studded Hz units to stick together and subsequently merge during Hz growth, which might
261 explain the absence of motion in the parasite's FV (Fig. 3*G*). Non-rapamycin-treated *pv5-*
262 *3xHA:loxP* control parasites mainly formed regular Hz crystals, however 27.5% of the crystals
263 exhibited a modest degree of branching (Fig. 3*G* and *SI Appendix*, Table S1). Furthermore,
264 crystal size and aspect ratio were reduced in comparison to WT parasites, together suggesting
265 a moderate functional impairment of 3xHA-tagged *Pf*PV5 (Fig. 3*G* and *SI Appendix*, Table
266 S1).

267 To determine whether *Pf*PV5 loss impacts on haemoglobin digestion, we examined
268 the haemoglobin content of synchronous saponin-released *pv5-3xHA:loxP* parasites. We
269 found that rings and trophozoites contained normal amounts of intraparasitic haemoglobin in
270 the absence of *Pf*PV5 (*SI Appendix*, Fig. S5*A*). By contrast, *Pf*PV5-deficient schizonts
271 exhibited a ~2-fold increase in levels of haemoglobin. Despite this, we observed no vacuolar
272 bloating as seen in parasites where haemoglobin catabolism is blocked by the protease
273 inhibitor E64, suggesting that the slightly elevated haemoglobin levels in the absence of *Pf*PV5
274 fall within the range of residual substrate and do not contribute to the observed defects (*SI*
275 *Appendix*, Fig. S5*B*). Furthermore, treatment of WT parasites with E64 produced no changes
276 in the architecture of Hz (*SI Appendix*, Fig. S5*C*). Our data thus show that PV5 regulates Hz
277 morphogenesis in *P. falciparum* independent of haemoglobin breakdown.

278 **Pb*PV5* expression influences antimalarial drug sensitivity *in vivo***

279 In the light of our evidence implicating PV5 in Hz formation, we next tested whether parasites
280 with affected PV5 function display altered sensitivity towards chloroquine, a 4-aminoquinoline
281 which is thought to inhibit biomineralization in *Plasmodium* (22-25). The absence of *Pf*PV5 did
282 not detectably alter chloroquine sensitivity in cultured *P. falciparum* parasites (*SI Appendix*,
283 Fig. S4*D*). In stark contrast to this, however, the *P. berghei* promoter swap mutants responded
284 to drug treatment slightly earlier and disappeared from the circulation much more rapidly than
285 WT parasites (Fig. 4*A*). A similar phenotype was observed upon treatment of infected mice
286 with the artemisinin derivative artesunate, also previously been implicated in haem
287 sequestration, although this remains contentious (35-39) (Fig. 4*B*). Most surprisingly, we also
288 observed marked hypersensitivity of the *P. berghei* mutants towards atovaquone, a compound
289 that targets the parasite's mitochondrial electron transport chain (Fig. 4*C*), as well as a slight

290 but non-significant increase in sensitivity towards the antifolate sulfadoxin (Fig. 4*D*). The
291 relative survival levels of *pv5::5'ptex88* and *pv5::5'hsp101* on the fourth day of drug treatment
292 suggested the greatest degree of hypersensitivity towards chloroquine (2.1% and 1.4% of WT
293 survival, respectively), followed by atovaquone (3.5% and 8.6%) and artesunate (4.4% and
294 9.9%), and eventually sulfadoxin (20.5% and 27.8%). Collectively, these results suggest that
295 interference with *PV5* expression critically enhances vulnerability of the parasite towards drug-
296 mediated insult during *in vivo* blood infection.

297 **DISCUSSION**

298 In this work, we have demonstrated that Hz formation in malaria parasites involves a secreted
299 calycin family member called PV5. While transcriptional deregulation of *PV5* in *P. berghei*
300 resulted in protracted Hz elongation along a pre-existing crystal plane, multidirectional
301 branching was observed in the complete absence of PV5 in *P. falciparum*. Species differences
302 aside, the disparity between those two phenotypes can be explained by the unique
303 transcriptional dynamics observed in the *P. berghei* mutants. Here, the hyperactive crystal
304 elongation, that follows an initial phase of normal Hz growth, coincides with a substantial
305 increase in Pb*PV5* transcript abundance during late parasite development. Together with the
306 chaotic Hz crystal branching observed in PV5-deficient *P. falciparum* parasites, this leads us
307 to propose that PV5 acts as a facilitator of unidirectional Hz extension.

308 It is interesting to speculate on the mechanisms by which PV5 may partake in haem
309 biomineralization. In laboratory crystallization experiments, the extent of crystallographic
310 mismatch branching is highly dependent on the degree of solute supersaturation, with high
311 levels favouring the generation of novel crystal nuclei on the surface of the parent crystal (40).
312 By contrast, lower degrees of supersaturation usually promote the expansion of pre-existing
313 crystals (40). It is conceivable that PV5 might reduce the extent of haem supersaturation by
314 binding haem or haematin dimers, thereby moderating *de novo* Hz nucleation and promoting
315 unidirectional crystal elongation. This could explain the Hz branching upon loss of PV5 in *P.*
316 *falciparum* as well as the prolonged crystal elongation and reduced Hz production upon late
317 upregulation of *PV5* in the *P. berghei* mutants. In support of this model, some lipocalin family
318 members are known to specifically bind the haem degradation product biliverdin (41-43). Such
319 interactions are unlikely to occur within the predicted PV5 β-barrel due to spatial constraints.
320 However, although experimental validation for this is currently lacking, potential ligand binding
321 sites might be located at the predicted prominently exposed loop between the barrel's β-
322 strands 5 and 6 (Fig. 1*B*) or at the extended amino-terminus.

323 The crystal branching characterising PV5-deficient *P. falciparum* parasites could also
324 be elicited by non-haem impurities adsorbing onto the crystal surface where they would
325 generate novel nucleation sites (40). In this alternative functional model, PV5 could act to bind
326 these impurities to create a vacuolar environment permissive for proper biomineralization.
327 *Pf*PV5-deficient parasites maintain an intact FV with a trans-vacuolar proton gradient as
328 indicated by staining with the acidotropic dye Lysosensor Blue DND-167 (*SI Appendix*, Fig.
329 S6*A*). In the absence of indications for FV membrane damage, differences in leakage of
330 impurities from the parasite cytoplasm can be dismissed. However, we cannot rule out the

331 possibility that specific ions or organic compounds are more abundant in the vacuolar matrix
332 of PV5-deficient parasites.

333 While the exact biophysical mechanisms that govern PV5-mediated Hz
334 morphogenesis remain to be delineated, our results support a model of conventional
335 crystallization within the aqueous milieu of the parasite's digestive compartments. The distinct
336 changes in crystal morphology and branching behaviour in the *PV5* mutants concur with
337 established mineralogical phenomena and are difficult to reconcile with a lipid or protein-
338 mediated polymerization scenario.

339 The striking dual localization pattern of PV5 is suggestive of initial secretion into the
340 PV followed by endocytic uptake. Surprisingly, *Pf*PV5 did not ultimately localize to the Hz-
341 containing FV in *P. falciparum*, but was frequently detected in intraparasitic vesicular
342 structures. These vesicles likely reflect endosomal compartments, which have previously been
343 implicated as sites of Hz nucleation and early crystal growth (44). The apparent exclusion of
344 *Pf*PV5 from the FV might indicate recycling to the PV. We propose that the effects exerted by
345 *Pf*PV5 in these organelles are eventually maintained within the FV upon endosomal fusion,
346 where *Pf*PV5 activity is no longer required. The interdependency between early and late
347 endosomal compartments is further supported by the observation of transient vacuolar
348 swelling in the *P. berghei* mutants. Here, the inability to crystallize sufficient amounts of haem
349 within the DVs might lead to a delay in DV budding, resulting in enlarged haemoglobin-
350 containing FVs, and similar mechanisms are likely the cause for the residual haemoglobin in
351 the FV of *Pf*PV5-deficient *P. falciparum* schizonts. Accordingly, the Hz-inhibiting activities of
352 aminoquinolines and artemisinin have been shown to be accompanied by an inhibition of
353 endocytic trafficking and haemoglobin processing (45, 46).

354 Our previous experiments had indicated that Pb*PV5* is essential for the asexual blood
355 stage development of *P. berghei* (27), and the deregulation of Pb*PV5* transcription in the
356 mutants described here indeed led to a striking fitness cost during *in vivo* infection. By contrast,
357 complete ablation of Pf*PV5* in *P. falciparum* only resulted in a moderate fitness loss *in vitro*.
358 The apparent dispensability of Pf*PV5* is therefore puzzling, but can be resolved by the notion
359 that *in vitro* culture does not necessarily reflect all adversities encountered during host
360 infection. For instance, Hz-mediated stiffening of the residual body in the absence of PV5
361 might hinder the passage of infected cells through capillaries or through the inter-endothelial
362 slits of the spleen, a scenario that would result in parasite elimination only during *in vivo*
363 infection. Similarly, we observed enhanced drug susceptibility only in the *P. berghei* mutants.
364 Thus, it appears plausible, that any imbalance in haem biomineralization in the absence of
365 PV5 is compensated for under optimal culture conditions and unfolds its adverse effects only
366 during *in vivo* infection. We thus propose that the molecular mechanism by which PV5

367 regulates Hz formation might involve host factors that are not encountered in a cell culture
368 setting.

369 The observation of enhanced drug susceptibility in the Pb*PV5* mutants is in agreement
370 with the notion that aberrant haem biomineralization chemo-sensitizes parasites to partner
371 drugs. An attractive path for drug development would be the identification of specific PV5
372 inhibitors. Our results suggest that these would act synergistically with a range of antimalarials
373 *in vivo*, as shown here by elevated parasite clearance rates during infection with the Pb*PV5*
374 mutants. An unrelated slow-growing *P. berghei* mutant deficient in the maintenance of the
375 mitochondrial membrane potential displayed normal sensitivity towards atovaquone using the
376 same internally controlled assay (47), indicating that reduced parasite multiplication is unlikely
377 to cause drug hypersensitivity. Although oxidative stress and lipid peroxidation remained
378 unchanged upon deletion of Pf*PV5* (*SI Appendix*, Fig. S6*B*), the imbalance in haem
379 biomineralization suggests abnormal haem concentrations within the parasite mediating the
380 fitness loss and drug hypersensitivity.

381 Together, we provide the first conclusive evidence for a parasite factor involved in Hz
382 formation *in vivo*, called PV5. Since this parasite-encoded member of the calycin superfamily
383 also governs the parasites' vitality and susceptibility towards drug-mediated insult during blood
384 infection, our observations reinforce Hz formation as an attractive pathway for therapeutic
385 intervention with an emphasis on development of a universal synergistic partner drug for
386 antimalarial combination therapies.

387 **MATERIALS & METHODS**

388 **Structure homology modelling.** Structure homology modelling was performed using the
389 SWISS-MODEL server (48). *Pf*PV5 (residues 35-214) was aligned to the experimentally
390 validated structure of *Ec*Blc (residues 27-175, PDB ID: 3MBT) (49), resulting in a GMQE value
391 of 0.39 and a QMEAN value of -5.48. Modelling was confirmed with I-TASSER (50), which
392 also identified *Ec*Blc (PDB ID: 2ACO) (51) as the most closely related structural analogue of
393 *Pf*PV5 with a TM score of 0.75. Due to a lack of sequence similarity, the structure of the
394 extended *Pf*PV5 amino-terminus could not be modelled.

395 ***P. berghei* cultivation**. *P. berghei* parasites were propagated in SWISS mice under constant
396 drug pressure with pyrimethamine (70 mg/l in drinking water, ingested *ad libitum*, MP
397 Biomedicals) to avoid homology-induced reversion of the promoter swap mutants to the
398 original WT genotype. This was routinely checked by diagnostic PCR of genomic DNA as
399 shown in *SI Appendix*, Figures S2 *A* and *B*. Drug pressure was withdrawn 5 days prior to
400 experimentation to avoid secondary effects of pyrimethamine treatment. Pyrimethamine-
401 resistant Berred WT parasites (52) were treated accordingly. All infection experiments were
402 carried out in strict accordance with the German 'Tierschutzgesetz in der Fassung vom 22.
403 Juli 2009' and the Directive 2010/63/EU of the European Parliament and Council 'On the
404 protection of animals used for scientific purposes'. The protocol was approved by the ethics
405 committee of the Berlin state authority ('Landesamt fur Gesundheit und Soziales Berlin', permit
406 number G0294/15).

407 *P. berghei* growth was determined with the previously described intravital competition
408 assay (52). In short, 500 mCherry-fluorescent Berred WT and 500 GFP-fluorescent mutant
409 blood stage parasites were co-injected intravenously and parasitaemia was analysed daily by
410 flow cytometry. For drug sensitivity assays, $5x10^6$ WT and $5x10^6$ mutant parasites were co-
411 injected intravenously. Drug treatment as well as daily flow cytometric parasite detection were
412 commenced three days later (47). Mice were treated with curative doses of chloroquine (288
413 mg/l in drinking water, ingested *ad libitum*, Sigma Aldrich), atovaquone (1.44 mg/kg body
414 weight per day injected intraperitoneally; GlaxoSmithKline), artesunate (50 mg/kg body weight
415 per day injected intraperitoneally; Sigma Aldrich) or sulfadoxin (1.4 g/l in drinking water,
416 ingested *ad libitum*; Sigma Aldrich). Mixed blood stages and schizonts were purified by
417 nycodenz gradient centrifugation (53).

418 ***P. falciparum* cultivation**. *P. falciparum* parasites were propagated in type AB+ human red
419 blood cells at 90% N_2, 5% CO_2 and 5% O_2 at 37°C in RPMI 1640 containing AlbuMAXII

420 (Thermo Fisher Scientific) supplemented with 2 mM L-glutamine. Parasites were routinely
421 synchronized using a combination of percoll gradient centrifugation and sorbitol lysis and were
422 treated with 100 nM rapamycin, 21.7 µM E64 or equivalent volumes of dimethyl sulfoxide
423 (DMSO) from the early ring stage onward. Growth assays were performed as described
424 previously (54) and parasitaemia as well as DNA content were measured by flow cytometry
425 using the nuclear dye SYBR Green (1:10,000; Thermo Fisher Scientific). For invasion assays,
426 mature schizonts were incubated at 2% initial parasitaemia under static or shaking (120 rpm)
427 conditions, as confirmed by flow cytometry. Parasitaemia was measured again 24 hours after
428 inoculation and the fold-change was calculated. For drug-response analysis of *pv5-3xHA:loxP*
429 parasites, ring stage cultures at 0.5% parasitaemia were treated with varying concentrations
430 of chloroquine in the presence of DMSO or rapamycin. Parasitaemia was determined three
431 days later and the fold-change was calculated.

432 **Generation and validation of transgenic *Plasmodium* parasites**. To generate the Pb*PV5*
433 promoter swap mutants, the amino-terminal sequence of Pb*PV5* (PBANKA_0826700) was
434 PCR-amplified and cloned into the B3D+ vector using *BamH*I and *Sac*II. The promoters of
435 Pb*PTEX88* (PBANKA_0941300) or Pb*HSP101* (PBANKA_0931200) were then amplified and
436 cloned in front of the start codon using *BamH*I (*SI Appendix*, Figure S1*A*). Vectors were
437 linearized with *BstB*I and transfected into GFP-fluorescent *P. berghei* Bergreen WT parasites,
438 using standard protocols (53, 55, 56). Transgenic parasites were selected for with
439 pyrimethamine and isolated by limiting dilution cloning. Pb*PV5* transcript abundance in the
440 WT and the promoter swap mutants was measured by quantitative real-time PCR (qPCR) and
441 normalized to *Pb*S18 rRNA.

442 The conditional Pf*PV5* knockout line was generated using established Cas9-mediated
443 techniques. In short, *P. falciparum* 3D7 parasites constitutively expressing DiCre (B11 line)
444 were co-transfected with a pDC2 guide plasmid inducing Cas9-mediated double strand
445 cleavage of the Pf*PV5* locus (PF3D7_0925900), together with a linearized repair template (57-
446 59) (*SI Appendix*, Figure S3*A*). The template was generated by gene synthesis and contained
447 5' and 3' homology arms and a re-codonised 3xHA-tagged Pf*PV5* sequence. The endogenous
448 intron of Pf*PV5* was replaced with an artificial intron containing a *loxP* site (58). A second *loxP*
449 sequence was introduced behind the Pf*PV5* stop codon. Transgenic parasites were selected
450 for with WR99210 and cloned by limiting dilution, making use of a previously developed plaque
451 assay (60). Primers used for molecular cloning, diagnostic PCR, and qPCR are indicated in
452 Figure 3*A* an in *SI Appendix*, Table S2 and Figures S1*A* and S3*A*.

453 **Fluorescence microscopy.** The transgenic *P. berghei* parasite line *pv5-tag-GFP*^{PV} (27) was
454 imaged live using an AxioImager Z2 epifluorescence microscope equipped with an AxioCam
455 MR3 camera (Zeiss). For mechanical parasite expansion, 1-2 µl of infected blood were
456 incubated under a 22 x 40 mm coverslip for several minutes until erythrocyte lysis became
457 apparent. *P. falciparum pv5-3xHA:loxP* parasites were fixed in 4% formaldehyde and imaged
458 by immunofluorescence on an Eclipse Ni light microscope (Nikon) fitted with a C11440 digital
459 camera (Hamamatsu). Immunofluorescence analysis was performed with rat anti-HA (1:500;
460 Sigma Aldrich) and rabbit anti-SERA5 (1:500) (54) primary antibodies in combination with
461 appropriate fluorophore-coupled secondary antibodies (1:1,000; Thermo Fisher Scientific).
462 Stainings with Lysosensor Blue DND-167 (Thermo Fisher Scientific), BODIPY 581/591 C11
463 (Image-iT Lipid Peroxidation Kit, Thermo Fisher Scientific) and CellROX Green (Thermo
464 Fisher Scientific) were performed according to the manufacturer's instructions.

465 **Scanning electron microscopy.** Hz was isolated from nycodenz (*P. berghei*) or percoll (*P.*
466 *falciparum*) gradient-purified infected red blood cells. Cells were lysed in water at room
467 temperature for 20 minutes, followed by a 10-minute centrifugation step at 17,000 x *g*. The
468 pellet was resuspended in 2% SDS in water and centrifuged as above. Three more washing
469 steps with 2% SDS were then followed by three washing steps with distilled water, before the
470 crystals were resuspended and transferred onto round glass cover slips (12 mm), where they
471 were dried. Cover slips were mounted on SEM specimen stubs, sputter-coated, and then
472 imaged on a LEO 1430 (Zeiss) or on a Quanta FEG 250 scanning electron microscope
473 (Thermo Fisher Scientific).

474 **Transmission electron microscopy.** Infected erythrocytes were initially fixed in 2.5%
475 glutaraldehyde, embedded in beads of 2% agarose, fixed and contrasted with 1% osmium
476 tetroxide, and further contrasted *en bloc* using 0.5% uranyl acetate. Following dehydration in
477 a graded series of ethanol and propylene oxide, beads were embedded in epoxy resin and
478 cured at 60°C for at least 24 hours. 60 nm sections were made with a Reichert Ultracut S
479 ultramicrotome (Leica) using a diamond knife. Sections were retrieved on copper hexagonal
480 mesh grids, and stained with 2% uranyl acetate and Reynold's lead citrate before imaging on
481 an EM 900 transmission electron microscope (Zeiss) equipped with a wide-angle slow-scan
482 2K CCD camera (Tröndle Restlichtverstärkersysteme).

483 **Electron diffraction.** Purified Hz was added to glow-discharged Lacey carbon films on 400
484 mesh copper grids which were then transferred to a Vitrobot Mark IV plunge freezer (Thermo
485 Fisher Scientific) with 100% humidity at 7 ˚C. The grids were blotted for 3 seconds with blot
486 force 1 and plunge frozen in liquid ethane cooled by liquid nitrogen. Electron diffraction data

487 were collected on a Talos cryo-electron microscope (Thermo Fisher Scientific) operated at
488 200 keV equipped with a hybrid pixel Timepix detector (512 x 512 pixels, 55 x 55 µm pixel
489 size; Amsterdam Scientific Instruments). Still and rotation (70˚) datasets were collected with a
490 beam size of 2 µm. The recording time varied between 15 and 100 seconds. To determine the
491 resolution, a powder pattern of an aluminum diffraction standard was recorded.

492 Since the Hz crystals had a strong tendency to stick together, we measured diffraction data of
493 crystal clusters. For each individual data set, we determined the location of the central electron
494 beam and shifted the patterns to make the beams coincide. Since crystal clustering prevented
495 indexing of the diffraction data, the radial median and maximum intensities were determined
496 as a function of resolution. Hereafter, the WT and *pv5::5'hsp101* datasets were averaged and
497 normalized to the local background median intensity at 0.18 $Å^{-1}$.

498 **Subcellular fractionation and immunoblotting.** *P. falciparum* parasites were released from
499 erythrocytes by treatment with 0.15% saponin in PBS and were lysed and heated in Laemmli
500 buffer. Murine erythrocytes infected with the *pv5-tag-GFP*^{PV} or *exp2-mCherry P. berghei* lines
501 (61) were purified on a nycodenz gradient and lysed hypotonically for 1 hour on ice in 10 mM
502 TRIS-HCl, pH 7.5. *P. berghei* lysates were spun 50 minutes at 100,000 × *g*. Membrane pellets
503 were resuspended in 0.1 M Na_2CO_3 in PBS or in 1% Triton X-100 in PBS, respectively, and
504 spun 50 minutes at 100,000 × *g*. Equal amounts of these fractions and *pv5-3xHA:loxP* parasite
505 lysates were separated on SDS-polyacrylamide and transferred onto a nitrocellulose
506 membrane. Western blotting was performed using rat anti-mCherry (1:5,000; ChromoTek),
507 chicken anti-GFP (1:5,000; Abcam), rat anti-HA (1:1,000, Sigma Aldrich), rat anti-*Pf*BiP
508 (1:1,000) (62) and rabbit anti-human-haemoglobin-α primary antibodies (1:1,000, Abcam)
509 followed by chemiluminescence detection with horseradish peroxidase-coupled secondary
510 antibodies (1:10,000; Sigma Aldrich, or 1:5,000, Jackson ImmunoResearch).

511 **Quantitative Hz analysis.** *P. berghei* Hz was visualized and quantified in methanol-fixed
512 trophozoites by reflection contrast polarized light microscopy using a Leica DMR microscope
513 equipped with a ProgRes MF camera (Jenoptik) and the POL filter set 513813 (Leica). Cellular
514 granularity was approximated by quantification of side scattered light using an LSRFortessa
515 flow cytometer (BD Biosciences). Hz crystal dimensions were analysed using FIJI. Due to the
516 variation in the *P. berghei* mutant's crystal width, individual crystals were divided into nine
517 evenly spaced segments along the dominant axis. The width of each segment was determined
518 and the values were averaged. For the *pv5::5'hsp101* parent crystal and the crystal outgrowth,
519 transects were drawn through the central axis of either structure and their shared angle was

520 determined. Hz movement within the FV of *pv5-3xHA:loxP* parasites was imaged live 36 hours
521 following treatment with DMSO or rapamycin, respectively.

522 **REFERENCES**

523 1. A. G. Maier, K. Matuschewski, M. Zhang, M. Rug, *Plasmodium falciparum*. *Trends*
524 *Parasitol* **35**, 481-482 (2019).

525 2. P. A. Sigala, D. E. Goldberg, The peculiarities and paradoxes of *Plasmodium* heme
526 metabolism. *Annu Rev Microbiol* **68**, 259-278 (2014).

527 3. V. L. Lew, T. Tiffert, H. Ginsburg, Excess hemoglobin digestion and the osmotic
528 stability of *Plasmodium falciparum*-infected red blood cells. *Blood* **101**, 4189-4194
529 (2003).

530 4. D. E. Goldberg, A. F. Slater, A. Cerami, G. B. Henderson, Hemoglobin degradation in
531 the malaria parasite *Plasmodium falciparum*: an ordered process in a unique organelle.
532 *Proc Natl Acad Sci U S A* **87**, 2931-2935 (1990).

533 5. C. Slomianny, G. Prensier, P. Charet, [Comparative ultrastructural study of the process
534 of hemoglobin degradation by *P. berghei* (Vincke and Lips, 1948) as a function of the
535 state of maturity of the host cell]. *J Protozool* **32**, 1-5 (1985).

536 6. A. R. Dluzewski *et al.*, Formation of the food vacuole in *Plasmodium falciparum*: a
537 potential role for the 19 kDa fragment of merozoite surface protein 1 (MSP1(19)). *PLoS*
538 *One* **3**, e3085 (2008).

539 7. S. Kumar, U. Bandyopadhyay, Free heme toxicity and its detoxification systems in
540 human. *Toxicol Lett* **157**, 175-188 (2005).

541 8. S. Pagola, P. W. Stephens, D. S. Bohle, A. D. Kosar, S. K. Madsen, The structure of
542 malaria pigment beta-haematin. *Nature* **404**, 307-310 (2000).

543 9. A. F. Slater *et al.*, An iron-carboxylate bond links the heme units of malaria pigment.
544 *Proc Natl Acad Sci U S A* **88**, 325-329 (1991).

545 10. I. Weissbuch, L. Leiserowitz, Interplay between malaria, crystalline hemozoin
546 formation, and antimalarial drug action and design. *Chem Rev* **108**, 4899-4914 (2008).

547 11. M. Olivier, K. Van Den Ham, M. T. Shio, F. A. Kassa, S. Fougeray, Malarial pigment
548 hemozoin and the innate inflammatory response. *Front Immunol* **5**, 25 (2014).

549 12. T. J. Egan, W. W. Mavuso, K. K. Ncokazi, The mechanism of beta-hematin formation
550 in acetate solution. Parallels between hemozoin formation and biomineralization
551 processes. *Biochemistry* **40**, 204-213 (2001).

552 13. T. J. Egan, D. C. Ross, P. A. Adams, Quinoline anti-malarial drugs inhibit spontaneous
553 formation of beta-haematin (malaria pigment). *FEBS Lett* **352**, 54-57 (1994).

554 14. M. M. Chen, L. Shi, D. J. Sullivan, Jr., *Haemoproteus* and *Schistosoma* synthesize
555 heme polymers similar to *Plasmodium* hemozoin and beta-hematin. *Mol Biochem*
556 *Parasitol* **113**, 1-8 (2001).

557 15. A. Dorn, R. Stoffel, H. Matile, A. Bubendorf, R. G. Ridley, Malarial haemozoin/beta-
558 haematin supports haem polymerization in the absence of protein. *Nature* **374**, 269-
559 271 (1995).

560 16. D. Jani *et al.*, HDP – a novel heme detoxification protein from the malaria parasite.
561 *PLoS Pathog* **4**, e1000053 (2008).

562 17. D. J. Sullivan, Jr., I. Y. Gluzman, D. E. Goldberg, *Plasmodium* hemozoin formation
563 mediated by histidine-rich proteins. *Science* **271**, 219-222 (1996).

564 18. A. F. Slater, A. Cerami, Inhibition by chloroquine of a novel haem polymerase enzyme
565 activity in malaria trophozoites. *Nature* **355**, 167-169 (1992).

566 19. A. N. Hoang, R. D. Sandlin, A. Omar, T. J. Egan, D. W. Wright, The neutral lipid
567 composition present in the digestive vacuole of *Plasmodium falciparum* concentrates
568 heme and mediates beta-hematin formation with an unusually low activation energy.
569 *Biochemistry* **49**, 10107-10116 (2010).

570 20. M. A. Ambele, T. J. Egan, Neutral lipids associated with haemozoin mediate efficient
571 and rapid beta-haematin formation at physiological pH, temperature and ionic
572 composition. *Malar J* **11**, 337 (2012).

573 21. J. M. Pisciotta *et al.*, The role of neutral lipid nanospheres in *Plasmodium falciparum*
574 haem crystallization. *Biochem J* **402**, 197-204 (2007).

575 22. D. J. Sullivan, Jr., I. Y. Gluzman, D. G. Russell, D. E. Goldberg, On the molecular
576 mechanism of chloroquine's antimalarial action. *Proc Natl Acad Sci U S A* **93**, 11865-
577 11870 (1996).

578 23. K. N. Olafson, T. Q. Nguyen, J. D. Rimer, P. G. Vekilov, Antimalarials inhibit hematin
579 crystallization by unique drug-surface site interactions. *Proc Natl Acad Sci U S A* **114**,
580 7531-7536 (2017).

581 24. T. Herraiz, H. Guillen, D. Gonzalez-Pena, V. J. Aran, Antimalarial quinoline drugs
582 inhibit beta-hematin and increase free hemin catalyzing peroxidative reactions and
583 inhibition of cysteine proteases. *Sci Rep* **9**, 15398 (2019).

584 25. S. N. Cohen, K. O. Phifer, K. L. Yielding, Complex formation between chloroquine and
585 ferrihaemic acid *in vitro*, and its effect on the antimalarial action of chloroquine. *Nature*
586 **202**, 805-806 (1964).

587 26. U. D'Alessandro, H. Buttiens, History and importance of antimalarial drug resistance.
588 *Trop Med Int Health* **6**, 845-848 (2001).

589 27. J. M. Matz, K. Matuschewski, An *in silico* down-scaling approach uncovers novel
590 constituents of the *Plasmodium*-containing vacuole. *Sci Rep* **8**, 14055 (2018).

591 28. D. R. Flower, The lipocalin protein family: structure and function. *Biochem J* **318 (Pt**
592 **1)**, 1-14 (1996).

593 29. D. R. Flower, A. C. North, C. E. Sansom, The lipocalin protein family: structural and
594 sequence overview. *Biochim Biophys Acta* **1482**, 9-24 (2000).

595 30. H. E. Bullen *et al.*, Biosynthesis, localization, and macromolecular arrangement of the
596 *Plasmodium falciparum* translocon of exported proteins (PTEX). *J Biol Chem* **287**,
597 7871-7884 (2012).

598 31. M. Morita *et al.*, PV1, a novel *Plasmodium falciparum* merozoite dense granule protein,
599 interacts with exported protein in infected erythrocytes. *Sci Rep* **8**, 3696 (2018).

600 32. H. Iriko *et al.*, *Plasmodium falciparum* exported protein 1 is localized to dense granules
601 in merozoites. *Parasitol Int* **67**, 637-639 (2018).

602 33. T. D. Otto *et al.*, A comprehensive evaluation of rodent malaria parasite genomes and
603 gene expression. *BMC Biol* **12**, 86 (2014).

604 34. J. M. Matz *et al.*, *In vivo* function of PTEX88 in malaria parasite sequestration and
605 virulence. *Eukaryot Cell* **14**, 528-534 (2015).

606 35. Y. L. Hong, Y. Z. Yang, S. R. Meshnick, The interaction of artemisinin with malarial
607 hemozoin. *Mol Biochem Parasitol* **63**, 121-128 (1994).

608 36. R. K. Haynes *et al.*, Artemisinin antimalarials do not inhibit hemozoin formation.
609 *Antimicrob Agents Chemother* **47**, 1175 (2003).

610 37. W. Asawamahasakda, I. Ittarat, C. C. Chang, P. McElroy, S. R. Meshnick, Effects of
611 antimalarials and protease inhibitors on plasmodial hemozoin production. *Mol*
612 *Biochem Parasitol* **67**, 183-191 (1994).

613 38. A. V. Pandey, B. L. Tekwani, R. L. Singh, V. S. Chauhan, Artemisinin, an endoperoxide
614 antimalarial, disrupts the hemoglobin catabolism and heme detoxification systems in
615 malarial parasite. *J Biol Chem* **274**, 19383-19388 (1999).

616 39. N. Basilico, E. Pagani, D. Monti, P. Olliaro, D. Taramelli, A microtitre-based method
617 for measuring the haem polymerization inhibitory activity (HPIA) of antimalarial drugs.
618 *J Antimicrob Chemother* **42**, 55-60 (1998).

619 40. X. Y. Liu, "Heterogeneous nucleation and crystal network formation" in Crystal growth
620 of technologically important electronic materials, K. Byrappa, T. Ohachi, H. Klapper,
621 R. Fornari, Eds. (Allied Publishers PVT. Limited, New Delhi, 2003), pp. 118-135.

622 41. R. Huber *et al.*, Molecular structure of the bilin binding protein (BBP) from *Pieris*
623 *brassicae* after refinement at 2.0 Å resolution. *J Mol Biol* **198**, 499-513 (1987).

624 42. R. Huber *et al.*, Crystallization, crystal structure analysis and preliminary molecular
625 model of the bilin binding protein from the insect *Pieris brassicae*. *J Mol Biol* **195**, 423-
626 434 (1987).

627 43. H. M. Holden, W. R. Rypniewski, J. H. Law, I. Rayment, The molecular structure of
628 insecticyanin from the tobacco hornworm *Manduca sexta* L. at 2.6 Å resolution. *EMBO*
629 *J* **6**, 1565-1570 (1987).

630 44. N. Abu Bakar, N. Klonis, E. Hanssen, C. Chan, L. Tilley, Digestive-vacuole genesis
631 and endocytic processes in the early intraerythrocytic stages of *Plasmodium*
632 *falciparum*. *J Cell Sci* **123**, 441-450 (2010).

633 45. Y. Zhang, Inhibition of hemoglobin degradation in *Plasmodium falciparum* by
634 chloroquine and ammonium chloride. *Exp Parasitol* **64**, 322-327 (1987).

635 46. H. C. Hoppe *et al.*, Antimalarial quinolines and artemisinin inhibit endocytosis in
636 *Plasmodium falciparum*. *Antimicrob Agents Chemother* **48**, 2370-2378 (2004).

637 47. J. M. Matz, C. Goosmann, K. Matuschewski, T. W. A. Kooij, An unusual prohibitin
638 regulates malaria parasite mitochondrial membrane potential. *Cell Rep* **23**, 756-767
639 (2018).

640 48. A. Waterhouse *et al.*, SWISS-MODEL: homology modelling of protein structures and
641 complexes. *Nucleic Acids Res* **46**, W296-W303 (2018).

642 49. A. Schiefner, L. Chatwell, D. A. Breustedt, A. Skerra, Structural and biochemical
643 analyses reveal a monomeric state of the bacterial lipocalin Blc. *Acta Crystallogr D Biol*
644 *Crystallogr* **66**, 1308-1315 (2010).

645 50. J. Yang, Y. Zhang, Protein structure and function prediction using I-TASSER. *Curr*
646 *Protoc Bioinformatics* **52**, 5 8 1-5 8 15 (2015).

647 51. V. Campanacci, R. E. Bishop, S. Blangy, M. Tegoni, C. Cambillau, The membrane
648 bound bacterial lipocalin Blc is a functional dimer with binding preference for
649 lysophospholipids. *FEBS Lett* **580**, 4877-4883 (2006).

650 52. J. M. Matz, K. Matuschewski, T. W. Kooij, Two putative protein export regulators
651 promote *Plasmodium* blood stage development *in vivo*. *Mol Biochem Parasitol* **191**,
652 44-52 (2013).

653 53. C. J. Janse *et al.*, High efficiency transfection of *Plasmodium berghei* facilitates novel
654 selection procedures. *Mol Biochem Parasitol* **145**, 60-70 (2006).

655 54. R. Stallmach *et al.*, *Plasmodium falciparum* SERA5 plays a non-enzymatic role in the
656 malarial asexual blood-stage lifecycle. *Mol Microbiol* **96**, 368-387 (2015).

657 55. J. M. Matz, T. W. Kooij, Towards genome-wide experimental genetics in the *in vivo*
658 malaria model parasite *Plasmodium berghei*. *Pathog Glob Health* **109**, 46-60 (2015).

659 56. T. W. Kooij, M. M. Rauch, K. Matuschewski, Expansion of experimental genetics
660 approaches for *Plasmodium berghei* with versatile transfection vectors. *Mol Biochem*
661 *Parasitol* **185**, 19-26 (2012).

662 57. C. R. Collins *et al.*, Robust inducible Cre recombinase activity in the human malaria
663 parasite *Plasmodium falciparum* enables efficient gene deletion within a single asexual
664 erythrocytic growth cycle. *Mol Microbiol* **88**, 687-701 (2013).

665 58. M. L. Jones *et al.*, A versatile strategy for rapid conditional genome engineering using
666 *loxP* sites in a small synthetic intron in *Plasmodium falciparum*. *Sci Rep* **6**, 21800
667 (2016).

668 59. E. Knuepfer, M. Napiorkowska, C. van Ooij, A. A. Holder, Generating conditional gene
669 knockouts in *Plasmodium* – a toolkit to produce stable DiCre recombinase-expressing
670 parasite lines using CRISPR/Cas9. *Sci Rep* **7**, 3881 (2017).

671 60. J. A. Thomas *et al.*, Development and application of a simple plaque assay for the
672 human malaria parasite *Plasmodium falciparum*. *PLoS One* **11**, e0157873 (2016).

673 61. J. M. Matz *et al.*, The *Plasmodium berghei* translocon of exported proteins reveals
674 spatiotemporal dynamics of tubular extensions. *Sci Rep* **5**, 12532 (2015).

675 62. E. Knuepfer *et al.*, RON12, a novel *Plasmodium*-specific rhoptry neck protein important
676 for parasite proliferation. *Cell Microbiol* **16**, 657-672 (2014).

677 63. R. Buller, M. L. Peterson, Ö. Almarsson, L. Leiserowitz, Quinoline binding site on
678 malaria pigment crystal: a rational pathway for antimalaria drug design. *Cryst Growth*
679 *Des* **2**, 553-562 (2002).

680 64. J. Friesen *et al.*, Natural immunization against malaria: causal prophylaxis with
681 antibiotics. *Sci Transl Med* **2**, 40ra49 (2010).

682 **AUTHOR CONTRIBUTIONS**

683 JMM conceived the study and performed all experiments requiring genetic manipulation and
684 cultivation of *P. berghei* and *P. falciparum* parasites. JMM, BD, AB, PM, TS and LC contributed
685 to Hz analysis by SEM and TEM. TBB, EvG and JPA performed and analysed electron
686 diffraction experiments. KM and MJB contributed to data interpretation. The manuscript was
687 written by JMM with input from TBB, EvG, JPA, KM and MJB.

688 **ACKNOWLEDGEMENTS**

689 We thank Volker Brinkmann and Christian Goosmann (Max Planck Institute for Infection
690 Biology, Berlin) for assistance with reflection contrast polarized light microscopy and Darren
691 Flower (Aston University, Birmingham) and Leslie Leiserowitz (Weizmann Institute of Science,
692 Rehovot) for fruitful discussion. This work was supported by a stipend from the Deutsche
693 Forschungsgemeinschaft (DFG, project number 419345764 to JMM) and in part by funding to
694 JMM, LC, AB and MJB from the Francis Crick Institute, which receives its core funding from
695 Cancer Research UK (FC001043), the UK Medical Research Council (FC001043), and the
696 Wellcome Trust (FC001043). JMM, BD, PM, TS and KM were also supported by the Humboldt
697 University and by the Alliance Berlin Canberra ‘‘Crossing Boundaries: Molecular Interactions
698 in Malaria’’, which is co-funded by a grant from the DFG for the International Research Training
699 Group (IRTG) 2290 and the Australian National University. We further acknowledge funding
700 from the Swiss National Science Foundation (project 31003A_17002 to TBB and project
701 200021_165669 to TBB and JPA). We thank the Center for Cellular Imaging and
702 NanoAnalytics for support and use of the cryo-electron microscope.

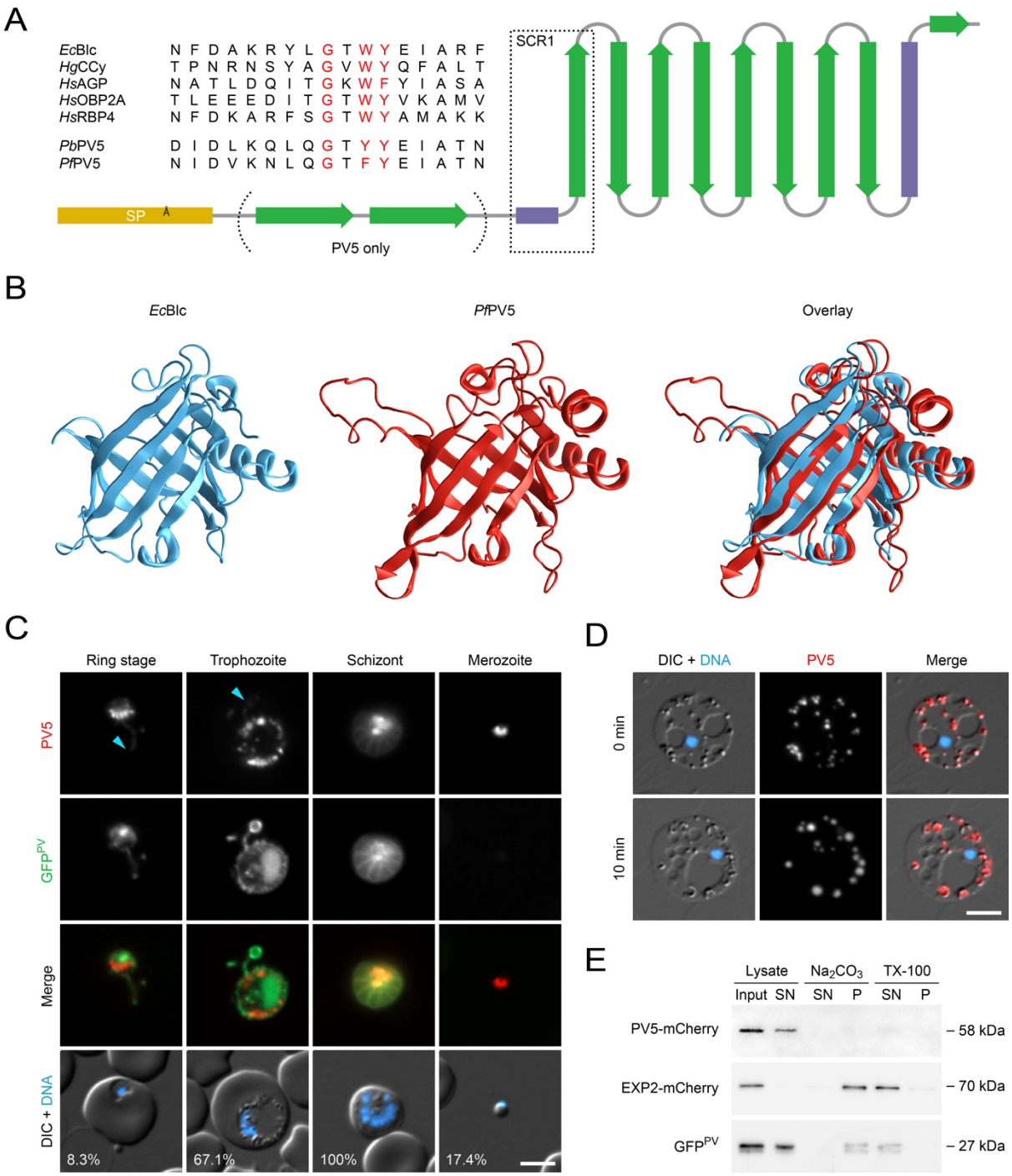

Fig. 1. The soluble lipocalin family member PV5 is trafficked to digestive vesicles in *Plasmodium berghei*.

(*A*) PV5 is a lipocalin family member. Secondary structure of *Plasmodium* PV5. Yellow, signal peptide (SP); green, ß-strands; purple, α-helices. Note the two amino-terminal ß-strands specific to PV5. Alignments of the structurally conserved region 1 (SCR1) from different lipocalin family members and PV5 are shown in the upper left corner. Signature residues are highlighted in red. *Ec*Blc, *Escherichia coli* bacterial lipocalin; *Hg*CCy; *Homarus gammarus* (European lobster) crustacyanin; *Hs*AGP, *Homo sapiens* α_1-acid glycoprotein;

712 *Hs*OBP2A, *H. sapiens* odorant-binding protein 2A; *Hs*RBP4, *H. sapiens* retinol-binding protein
713 4; *Pb*/*Pf*PV5, PV5 from *P. berghei* and *P. falciparum*.

714 (*B*) Structure homology modelling predicts a lipocalin fold for *Pf*PV5. Shown are the
715 experimentally validated structure of *Ec*Blc (blue, left, residues 27-175, PDB ID: 3MBT), the
716 derived model of *Pf*PV5 (red, centre, residues 35-214) using *Ec*Blc as a homology template,
717 and an overlay (right). Modelling was performed with SWISS-MODEL and supported by I-
718 TASSER. Amino acid sequence identity is 20%, similarity calculated from BLOSUM62
719 substitution matrix is 0.3.

720 (*C*) Dual protein localization of *Pb*PV5 to extensions of the parasitophorous vacuole (PV)
721 and to intraparasitic structures. Transgenic *P. berghei* parasites expressing the PV marker
722 GFP^{PV} and the endogenous Pb*PV5* gene fused to mCherry-3xMyc were imaged live (27).
723 Shown are the mCherry (first row) and GFP channels (second row), a merge of both signals
724 (third row) and a merge of differential interference contrast images (DIC) and Hoechst 33342
725 nuclear stain (fourth row). Cyan arrowheads, *Pb*PV5 in PV tubules. Numbers represent
726 normalized mCherry intensity values obtained by quantitative live fluorescence microscopy.
727 N=44 parasites.

728 (*D*) Intraparasitic *Pb*PV5 localizes to Hz-containing digestive vesicles (DVs). Parasites
729 were incubated in 1-2 µl under a large coverslip (22 x 40 mm) for several minutes, leading to
730 lysis of the host erythrocyte and the PV, and to mechanical expansion of the parasite (top).
731 Shown are a merge of differential interference contrast and Hoechst 33342 nuclear stain (first
732 row), the signal of tagged *Pb*PV5 (second row), as well as a merge of all three channels (third
733 row). Swelling of *Pb*PV5-containing DVs was observed ten minutes later (bottom). Note the
734 even distribution of *Pb*PV5 throughout the swollen DVs. Bars, 5 µm.

735 (*E*) *Pb*PV5 is a soluble protein. Subcellular fractionation was performed using the *Pb*PV5-
736 tagged parasite line, which also expresses the soluble marker GFP^{PV}, and a *P. berghei* line
737 expressing the transmembrane protein *Pb*EXP2 fused to mCherry-3xMyc (61). Cell lysates
738 were centrifuged and resultant membrane pellets were subjected to solubilization with Na_2CO_3
739 and Triton X-100 (TX-100). Input, supernatant (SN) and pellet fractions (P) were analysed by
740 Western blot using anti-mCherry and anti-GFP primary antibodies.

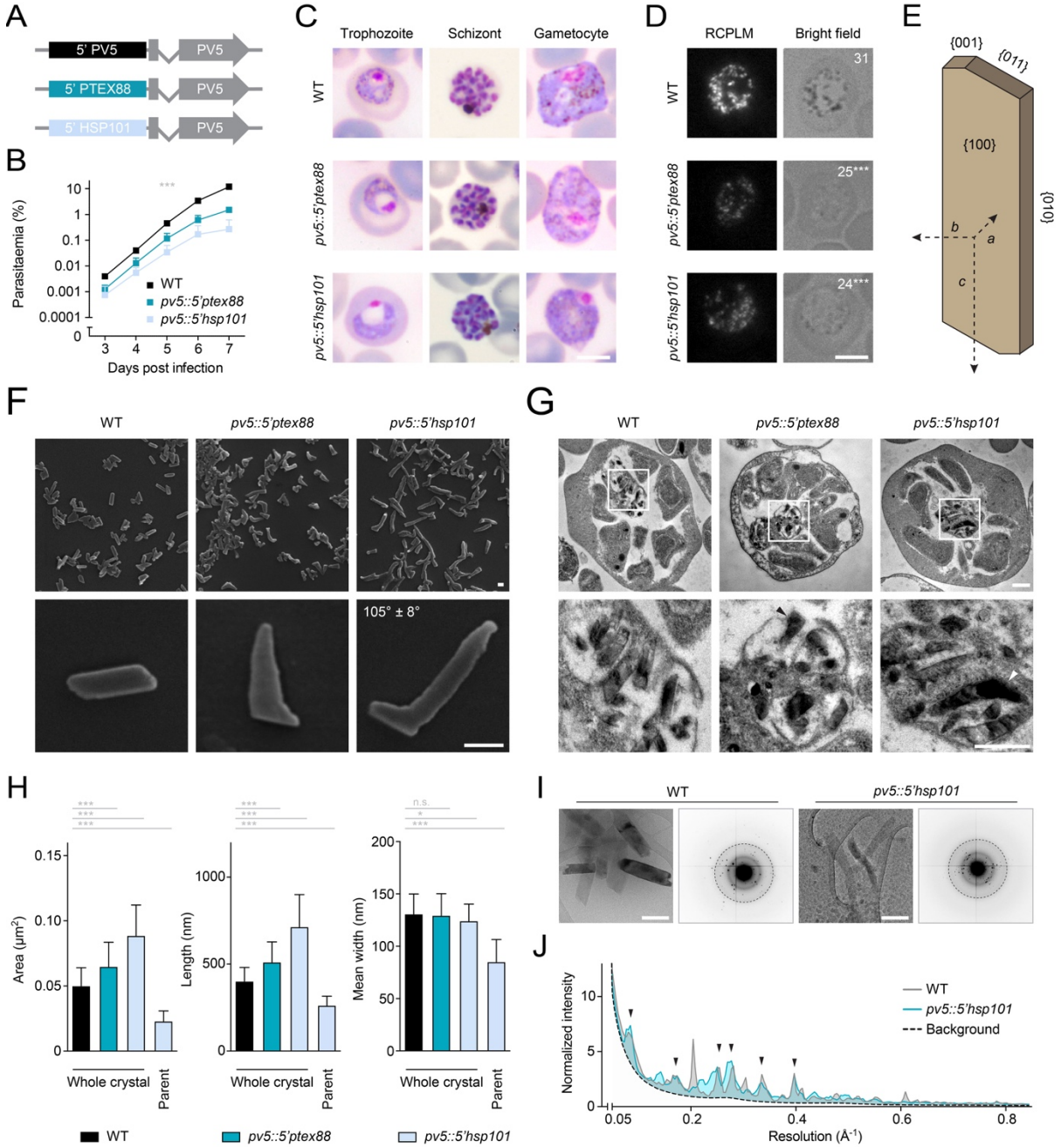

Fig. 2. Deregulated expression of *PV5* impacts haemozoin formation in *Plasmodium berghei.*

(*A*) Schematic representation of the genotypes of WT (top) and transgenic *pv5::5'ptex88* (middle) and *pv5::5'hsp101* parasites (bottom). In the mutants, the endogenous Pb*PV5* promoter (black) was exchanged for the promoter of Pb*PTEX88* (dark blue) or Pb*HSP101* (light blue) respectively.

(*B*) Reduced parasite proliferation upon *Pb*PV5 promoter swapping. Asexual blood stage development was analysed using the intravital competition assay (52). Average parasite multiplication rates were 11.4 (WT), 9.1 (*pv5::5'ptex88*) and 6.2 (*pv5::5'hsp101*). Shown are mean values +/- SD. ***, P<0.001; Two-way ANOVA. N=3 independent infections.

751 (*C*) Morphology of trophozoite, schizont and gametocyte stages in the WT, *pv5::5'ptex88*
752 and *pv5::5'hsp101* lines as observed by Giemsa staining. Note the lack of prominent dark
753 pigment granules in mutant trophozoites and gametocytes as well as the dilation of the central
754 food vacuole in mutant trophozoites. Bar, 5 µm.

755 (*D*) Pb*PV5* is required for efficient Hz formation. Trophozoites were visualized by reflection
756 contrast polarized light microscopy (RCPLM, left) and bright field imaging (right). Numbers
757 indicate the mean quantity of bright puncta in RCPLM images. Significances are shown for
758 the comparison of the mutants with WT. Bar, 5 µm. See also *SI Appendix*, Fig. S2*C*.

759 (E) Hz crystal architecture. In *Plasmodium* WT parasites, Hz assembles as triclinic high
760 aspect ratio parallelograms (63). Characteristic crystal axes and faces are indicated.

761 (*F*) Scanning electron micrographs of Hz purified from WT, *pv5::5'ptex88* and
762 *pv5::5'hsp101* mixed blood stage parasites. The angle between the regularly shaped
763 *pv5::5'hsp101* parent crystal and the outgrowth is indicated. N=130 crystals. Bars, 100 nm.

764 (*G*) Crystal morphology *in situ*. Shown are TEM images of WT, *pv5::5'ptex88* and
765 *pv5::5'hsp101* schizonts (top) as well as their residual body at higher magnification (bottom).
766 Abnormal crystal shapes in the mutants are indicated by arrowheads. Bars, 500 nm.

767 (*H*) Hyperactive Hz growth is unidirectional. Shown are the dimensions of whole individual
768 Hz crystals extracted from WT, *pv5::5'ptex88* and *pv5::5'hsp101* parasites including the area
769 exposed to the electron beam (left) as well as the length (centre) and mean width of the
770 crystals (right). The theoretical dimensions of the *pv5::5'hsp101* parent crystal were
771 interpolated and are depicted as well. n.s., non-significant; *, $P<0.05$; ***, $P<0.001$; One-way
772 ANOVA and Tukey's multiple comparison test. N=100 crystals.

773 (*I, J*) Unaltered crystalline order in Hz of *pv5::5'hsp101* parasites. (*I*) Depicted are TEM
774 images (left) of Hz purified from WT and *pv5::5'hsp101* parasites as well as their
775 corresponding electron diffraction patterns (right) showing comparable resolution of the Bragg
776 peaks. Dashed circles demark a resolution of 0.5 $Å^{-1}$. Bars, 200 nm. (*J*) Plot of the radial
777 maximum diffracted intensity as a function of resolution. Data were normalized to the average
778 median intensity at 0.18 $Å^{-1}$, in order to correct for differences in diffracted volume. Arrowheads
779 denote overlapping peaks. N=10 (WT) and 18 (*pv5::5'hsp101*) diffraction data sets.

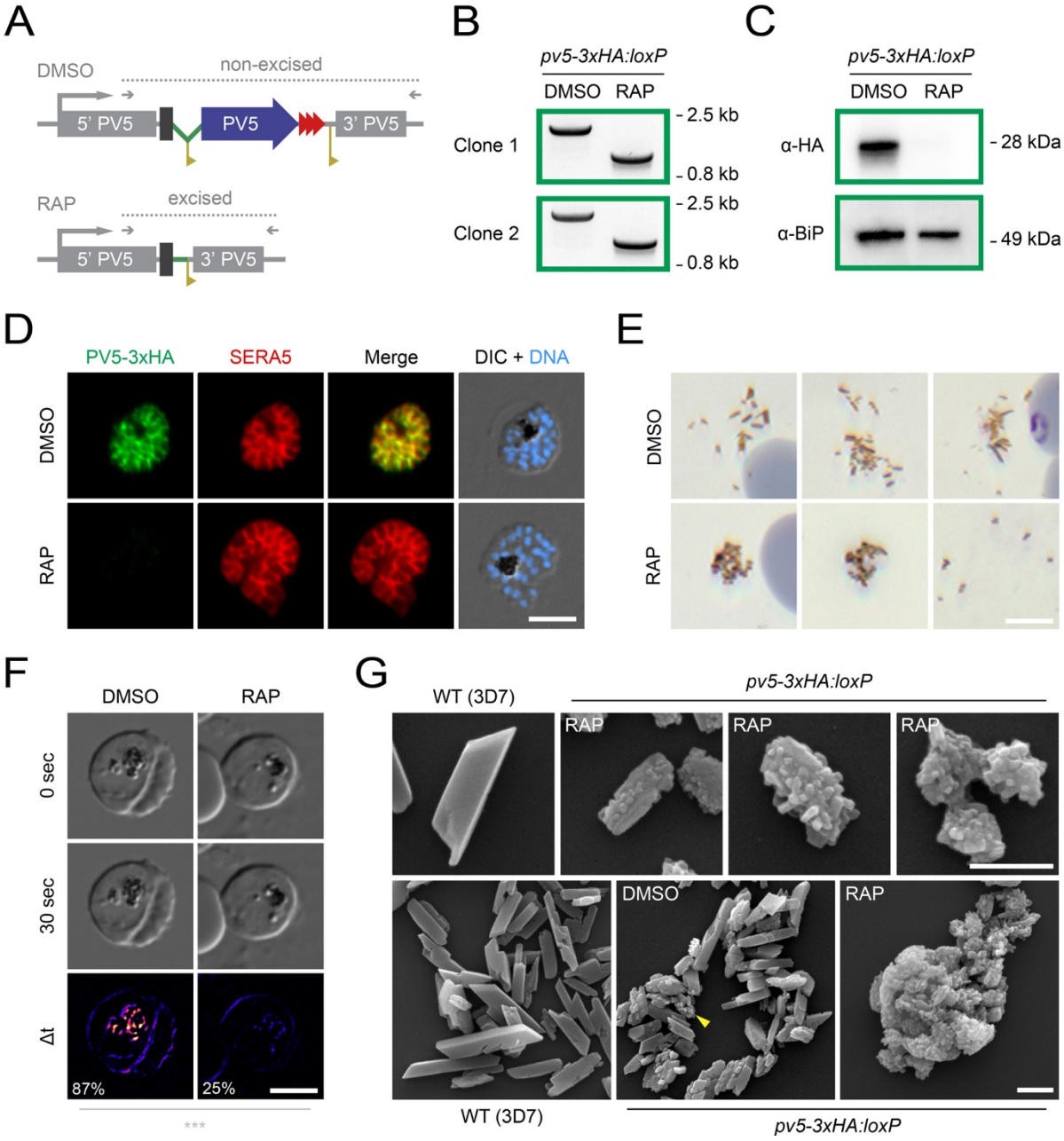

Fig. 3. Absence of PV5 causes haemozoin branching in *Plasmodium falciparum*.

(*A*) Schematic representation of DiCre-mediated Pf*PV5* excision. The endogenous locus was modified to introduce *loxP* sites (yellow) flanking the majority of the coding sequence of the 3xHA (red)-tagged *Pf*PV5 (blue). The artificial intron is indicated in green. See also *SI Appendix*, Fig. S3*A*. Treatment with rapamycin (RAP) induces Cre recombinase-mediated excision of the *loxP*-flanked sequence which results in truncation of Pf*PV5* leaving behind only the sequence encoding the protein's signal peptide. Excision-sensitive primer combinations are indicated by arrows and expected diagnostic PCR fragments by dotted lines.

(*B*) Diagnostic PCR of the Pf*PV5* locus following treatment with dimethyl sulfoxide (DMSO)

790 or RAP, respectively, using the primer combinations depicted in *A*. Results are shown from
791 two independent *pv5::3xHA:loxP* clones.

792 (*C*, *D*) Loss of *Pf*PV5 protein. (*C*) Western blot analysis of parasite extracts following
793 treatment with DMSO or RAP, respectively, using anti-HA and anti-*Pf*BiP primary antibodies.
794 (D) Immunofluorescence analysis was performed with primary antibodies directed against HA
795 and the PV protein *Pf*SERA5. Shown are the individual signals of tagged *Pf*PV5 (green, first
796 row) and *Pf*SERA5 (red, second row), a merge of both signals (third row) as well as a merge
797 of differential interference contrast images (DIC) with Hoechst 33342 nuclear stain (fourth row)
798 following treatment with DMSO or RAP, respectively. Bar, 5 µm.

799 (*E*) Abnormal Hz morphology in the absence of *Pf*PV5. Hz released from residual bodies
800 during parasite egress was imaged in Giemsa-stained thin culture smears of DMSO and RAP-
801 treated *pv5::3xHA:loxP* parasites. Note the spreading of elongated Hz crystals in DMSO-
802 treated cultures and the clumping of granular Hz upon RAP treatment. Only in very few
803 instances did the crystals detach from one another in RAP-treated cultures (last panel). Bar,
804 5 µm.

805 (*F*) Reduced Hz movement in the digestive vacuole upon loss of *Pf*PV5. Shown are DIC
806 images of live DMSO and RAP-treated *pv5::3xHA:loxP* parasites 36 hours after invasion.
807 Parasites were imaged twice at an interval of 30 seconds (top and centre) and the difference
808 of both images visualized with pixel-by-pixel intensity subtraction (bottom). Note the absence
809 of Hz movement in the RAP-treated parasite (see also *SI Appendix*, Movie S1). The
810 percentage of parasites with moving Hz is indicated. ***, $P<0.001$; Student's *t*-test. N=4
811 independent experiments with >300 parasites each. Bar, 5 µm.

812 (*G*) Scanning electron micrographs of Hz purified from WT and from DMSO or RAP-
813 treated *pv5::3xHA:loxP* schizonts. Bars, 500 nm.

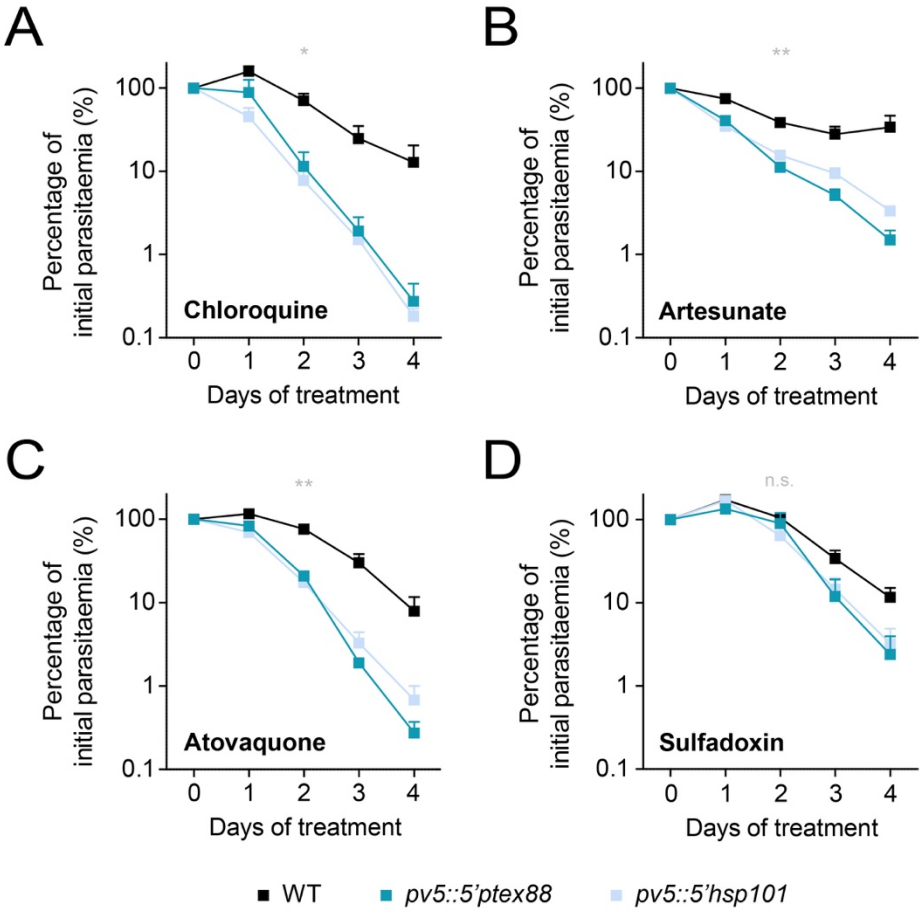

Fig. 4. Targeting Pb*PV5* function results in parasite hypersensitivity towards antimalarial drugs *in vivo*.

(*A-D*) 5 x 10^6 mCherry-fluorescent *P. berghei* WT parasites were injected into SWISS mice together with 5 x 10^6 GFP-fluorescent *pv5::5'ptex88* or *pv5::5'hsp101* parasites, respectively. From day three onward, mice were treated with curative doses of (*A*) chloroquine (288 mg/l in drinking water, *ad libitum*), (*B*) artesunate (50 mg/kg body weight, i.p.), (*C*) atovaquone (1.44 mg/kg body weight, i.p.) or (*D*) sulfadoxin (1.4 g/l in drinking water, *ad libitum*) and the respective parasitaemias were determined daily by flow cytometry of peripheral blood (47). Values are normalized to the parasitaemias on day 0 of treatment. Shown are mean values +/- SEM. n.s., non-significant; *, P<0.05; **, P<0.01; Two-way ANOVA. N=3 independent infections.

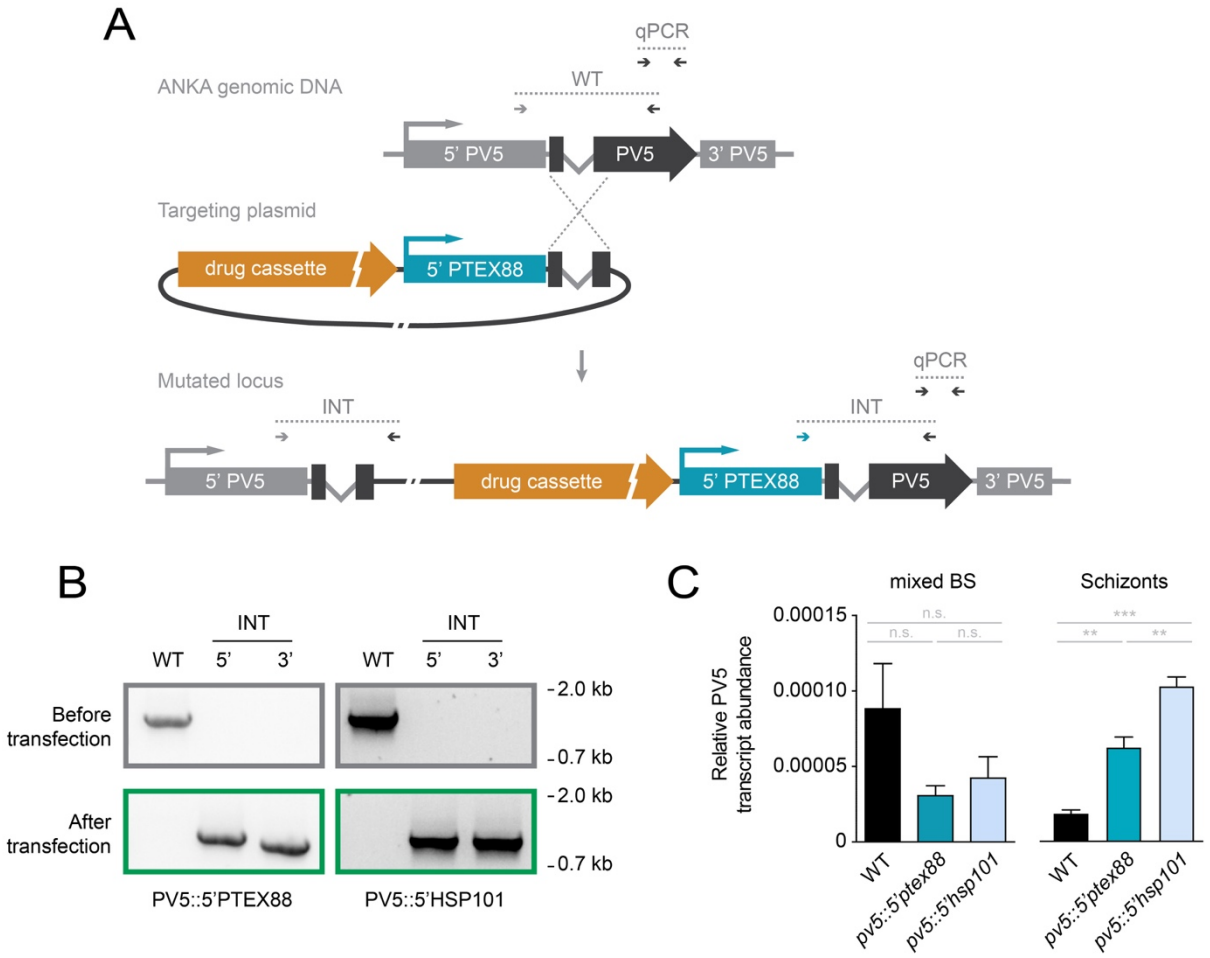

Fig. S1. Generation and validation of Pb*PV5* promoter swap mutants.

(*A*) Genetic strategy to exchange the endogenous promoter (light grey) of Pb*PV5* (dark grey) using single homologous recombination. The endogenous Pb*PV5* locus was targeted with an insertion plasmid containing the promoter sequence of Pb*PTEX88* (shown, blue) or Pb*HSP101* (not shown) fused to the amino-terminal sequence of Pb*PV5* as well as the drug-selectable hDHFR-yFcu cassette (orange). Successful insertion yields parasites expressing full length Pb*PV5* from a heterologous promoter and a non-functional amino-terminal fragment from the endogenous promoter, encoding the *Pb*PV5 signal peptide. Primer combinations for wild-type (WT) and integration-specific reactions (INT) as well as for quantitative real-time PCR (qPCR) are indicated by arrows and expected amplicons by dotted lines.

(*B*) Diagnostic PCR of the WT locus (top) and of the drug-selected and isolated Pb*PV5* mutants (bottom) using the primer combinations depicted in *A*.

(*C*) Dynamic changes in Pb*PV5* transcription upon promoter swap. Mixed blood stages (BS) and mature segmented schizonts were purified from mouse blood or from *in vitro* culture, respectively, and subjected to qPCR using primers targeting a carboxy-terminal portion of

842 Pb*PV5*, as depicted in *A*. Pb*PV5* transcript abundance was normalized to *Pb*18S rRNA.
843 Shown are mean values +/- SEM. n.s., non-significant; **, P<0.01; ***, P<0.001; One-way
844 ANOVA and Tukey's multiple comparison test. N=6 for mixed blood stages and 3 for schizonts.

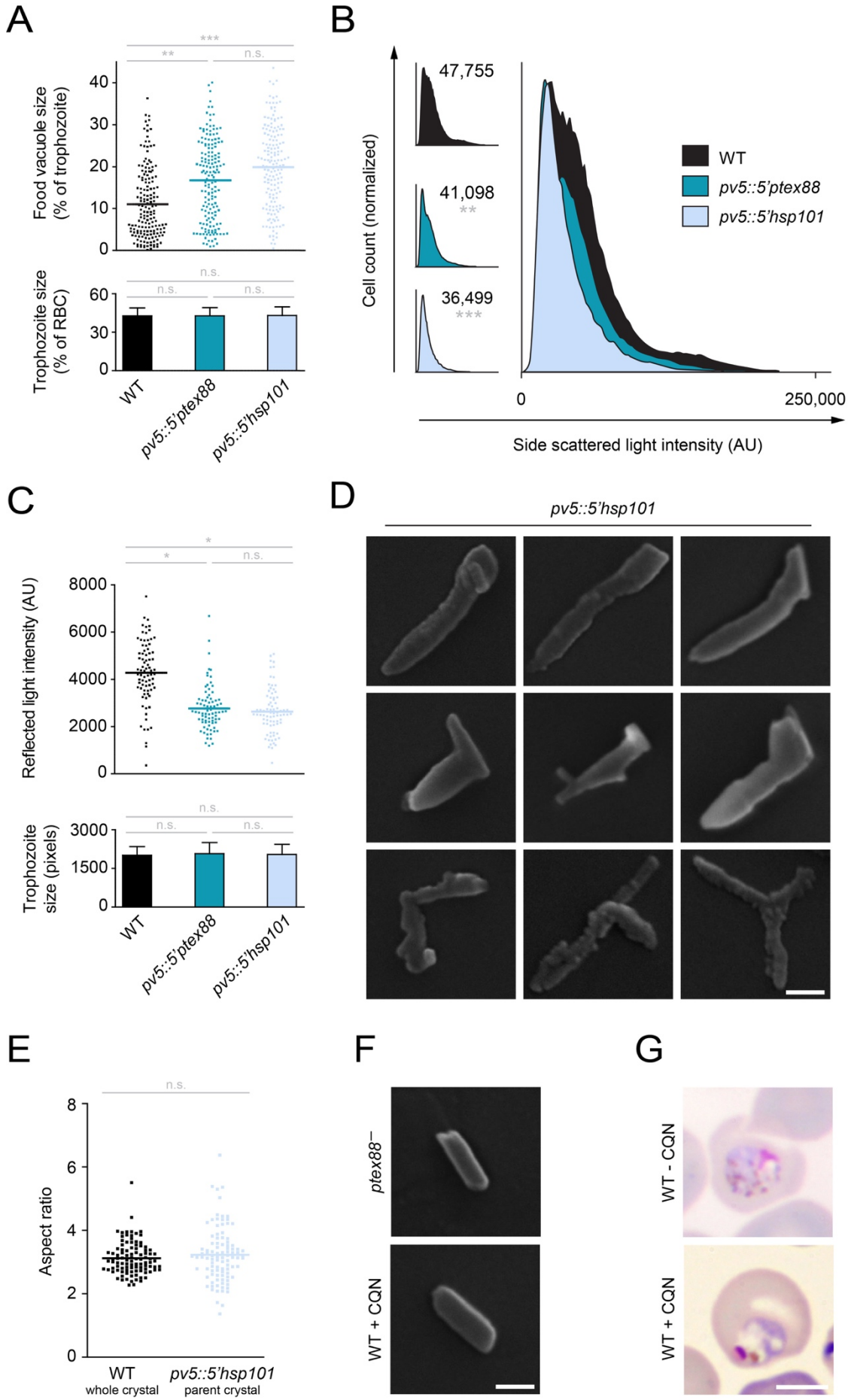
A
Food vacuole size (% of trophozoite)
Trophozoite size (% of RBC)
WT
pv5::5'ptex88
pv5::5'hsp101
B
Cell count (normalized)
47,755
41,098
36,499
WT
pv5::5'ptex88
pv5::5'hsp101
0
250,000
Side scattered light intensity (AU)
C
Reflected light intensity (AU)
Trophozoite size (pixels)
D
pv5::5'hsp101
E
Aspect ratio
WT
whole crystal
pv5::5'hsp101
parent crystal
F
ptex88−
WT + CQN
G
WT - CQN
WT + CQN

845

846 **Fig. S2.** Vacuolar dilation and defective haemozoin formation in the Pb*PV5* mutants.

847 (*A*) Quantification of vacuolar dilation. The translucent area observed in Giemsa-stained
848 trophozoites corresponding to the food vacuole was measured microscopically and expressed
849 as the percentage of the entire trophozoite area (upper graph). Depicted are individual and
850 mean values (bars). Only trophozoites of identical size were analysed (lower graph). Shown
851 are mean values +/- SD. n.s., non-significant; **, P<0.01; ***, P<0.001; One-way ANOVA and
852 Tukey's multiple comparison test. N=165 trophozoites from 5 independent infections.

853 (*B*) Pb*PV5* promoter swap mutants are less granular. Infected blood was subjected to
854 flow cytometry and the intensity of the side scattered light was determined. Shown are
855 individual histograms including the mean side scatter intensity values (left) as well as a merge
856 of WT, *pv5::5'ptex88* and *pv5::5'hsp101* histograms (right). Significances are shown for the
857 comparison of the mutants with WT. n.s., non-significant; **, P<0.01; ***, P<0.001; One-way
858 ANOVA and Tukey's multiple comparison test. N=6 independent infections.

859 (*C*) Quantitative reflection contrast polarized light microscopy. Depicted are individual and
860 mean intensity values of reflected light in methanol-fixed WT, *pv5::5'ptex88* and *pv5::5'hsp101*
861 trophozoites (bars, upper graph). Only trophozoites of similar size were analysed (lower
862 graph). Depicted are mean values +/- SD. n.s., non-significant; *, P<0.05; One-way ANOVA
863 and Tukey's multiple comparison test. N=80 trophozoites from 4 independent infections.

864 (*D*) A selection of Hz crystals generated by *pv5::5'hsp101* parasites as visualized by
865 scanning electron microscopy. Bar, 100 nm.

866 (*E*) Normal aspect ratio of *pv5::5'hsp101* parent crystals. Shown are the aspect ratios of
867 whole Hz crystals from WT parasites and of the parent crystal from *pv5::5'hsp101*-generated
868 Hz. Depicted are individual and mean values (bars). n.s., non-significant; Student's *t*-test.
869 N=100 crystals.

870 (*F*, *G*) Hz morphology is not affected by slow parasite growth or mortality. (*F*) Crystals
871 were extracted from slow-growing *PTEX88* knockout parasites (top) and from WT parasites
872 treated with curative doses of chloroquine (CQN, 288 mg/l in drinking water, *ad libitum*)
873 (bottom) and were visualized by scanning electron microscopy. Bar, 100 nm. (*G*) Morphology
874 of untreated (top) and CQN-treated WT parasites (bottom) as shown by Giemsa staining. Note
875 the pigment clumping and vesiculation in the dying parasite. Bar, 5 µm.

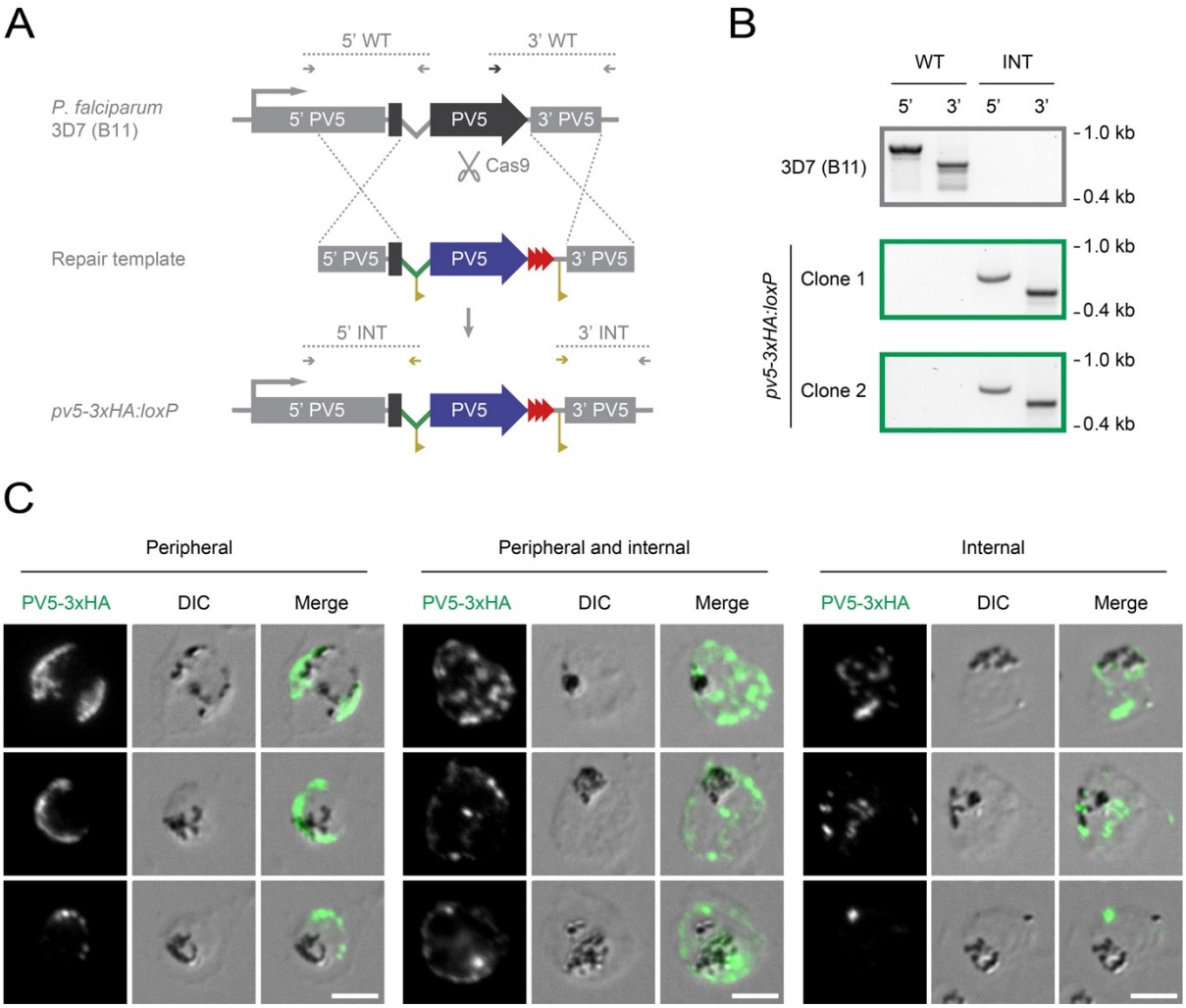

Fig. S3. PV5 localizes to the parasitophorous vacuole and to intraparasitic structures in *Plasmodium falciparum*.

(*A*) Genetic strategy for the generation of a conditional Pf*PV5* knockout line. The endogenous Pf*PV5* locus (dark grey) was targeted by Cas9-mediated double strand cleavage and repaired by homologous recombination with a synthetic template containing 5' and 3' homology arms (light grey), a 3xHA-tagged (red) re-codonised version of Pf*PV5* (blue) and *loxP* sequences (yellow) within the artificial intron (green) and behind the Pf*PV5* stop codon. Wild-type (WT) and integration-specific primer combinations (INT) are indicated by arrows and expected amplicons by dotted lines.

(*B*) Diagnostic PCR of the recipient *P. falciparum* 3D7 (B11) line (top) and of two isolated *pv5-3xHA:loxP* clones (bottom) using the primer combinations depicted in *A*.

(*C*) Dual localization of *Pf*PV5. Immunofluorescence analysis was performed using anti-HA primary antibodies. Depicted are exemplary *pv5-3xHA:loxP* trophozoites and young schizonts demonstrating localization of *Pf*PV5 exclusively to the parasitophorous vacuole (PV,

891 left), to the PV and internal parasite structures (centre) or to intraparasitic structures only
892 (right). Shown are the signal of tagged *Pf*PV5 (left columns), differential interference contrast
893 images (centre columns) and a merge (right columns). Bars, 5 µm.

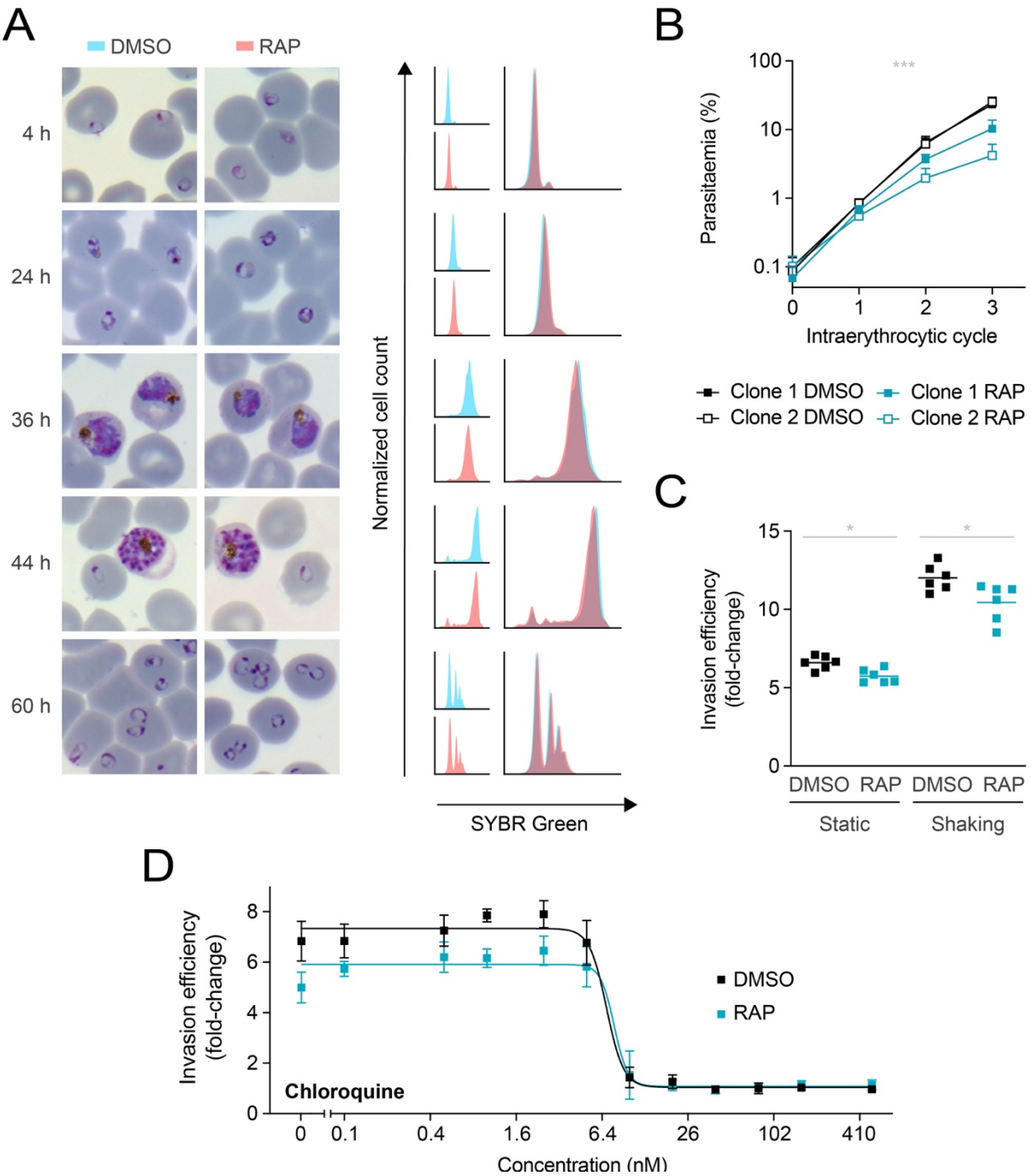

894

895 **Fig. S4.** Survival of *in vitro* cultivated *Plasmodium falciparum* in the absence of *Pf*PV5.

896 (*A*) *Pf*PV5-deficient parasites mature normally *in vitro*. Tightly synchronized
897 *pv5::3xHA:loxP* ring stages were treated with dimethyl sulfoxide (DMSO, blue) or rapamycin
898 (RAP, red) and then visualized by Giemsa staining 4, 24, 36, 44 and 60 hours later (left). In
899 parallel, nuclear SYBR Green fluorescence was quantified by flow cytometry. Individual and
900 merged histograms are depicted. Results are representative of two independent experiments.

901 (*B*) Asexual parasite proliferation is impaired upon loss of *Pf*PV5. Shown are growth
902 curves of two independent *pv5::3xHA:loxP* clonal lines upon treatment with DMSO or RAP,

903 respectively. Averaged parasite multiplication rates are 7.6 (DMSO) and 4.6 (RAP). Shown
904 are mean values +/- SD. ***, P<0.001; Two-way ANOVA. N=6 independent infections.

905 (*C*) Impaired schizont to ring stage transition in the absence of *Pf*PV5. Schizonts from
906 DMSO- and RAP-treated *pv5::3xHA:loxP* cultures were added to fresh erythrocytes and
907 incubated under static or shaking conditions for 24 hours. Shown is the fold-change in
908 parasitaemia, depicted as individual and mean values (bars). *, P<0.05; paired *t*-test. N=6
909 independent infections.

910 (*D*) *Pf*PV5-deficient parasites retain normal sensitivity towards chloroquine. Shown is a
911 dose-response analysis of DMSO- and RAP-treated *pv5::3xHA:loxP* parasites. Static ring
912 stage cultures were treated with varying chloroquine concentrations and the transition into the
913 following intraerythrocytic cycle was quantified. Depicted are mean values (+/- SD). N=3. Non-
914 linear regression analysis yielded IC_{50} values of 6.9 nM (DMSO) and 7.8 nM (RAP).

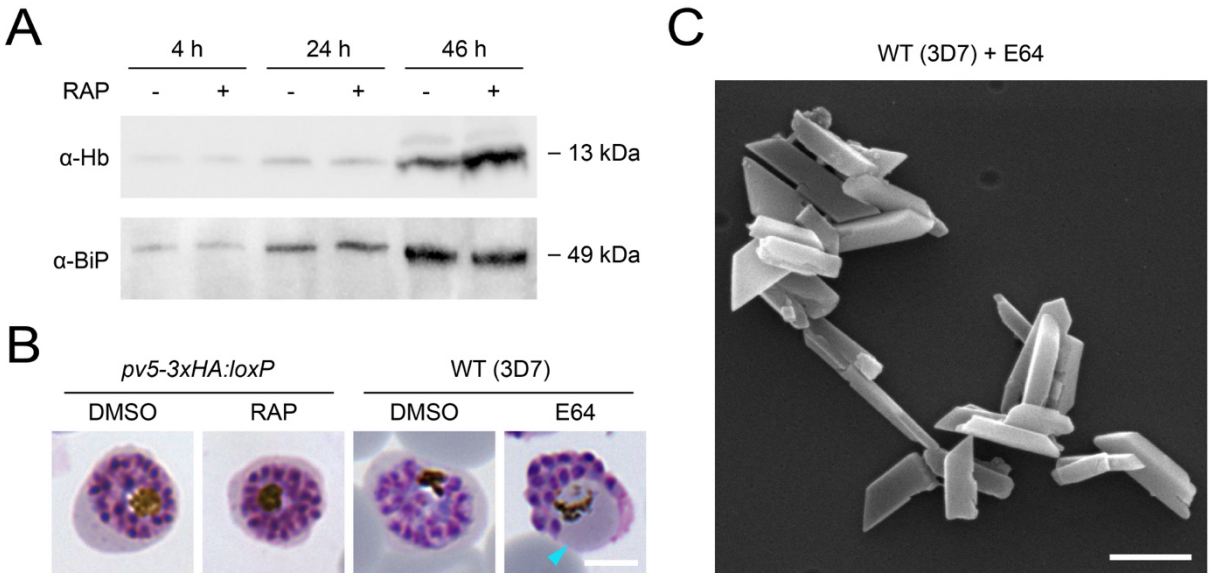

Fig. S5. Effective haemoglobin digestion in the absence of *Pf*PV5.

(*A*) Western blot analysis of induced and non-induced *pv5-3xHA:loxP* parasites released from their host cells by saponin lysis at the indicated timepoints after invasion. Blots were probed with antibodies directed against human haemoglobin α (Hb, top) and *Pf*BiP (bottom). Densitometry suggests that RAP-treated *pv5-3xHA:loxP* parasites contain 104% (4 h), 93% (24 h) and 203% (46 h) of intact internalized haemoglobin α in comparison to non-induced parasites.

(*B*) *Pf*PV5-deficient schizonts exhibit no vacuolar bloating. Shown are *pv5-3xHA:loxP* parasites treated from the ring stage onward with dimethyl sulfoxide (DMSO) or rapamycin (RAP) and *Plasmodium falciparum* WT parasites treated from 24 hours post invasion onward with DMSO or E64. Cyan arrowhead, bloated food vacuole. Bar, 5 µm.

(*C*) Inhibition of haemoglobin catabolism does not result in abnormal Hz morphology. Shown is a scanning electron micrograph of Hz crystals isolated from the E64-treated *P. falciparum* WT parasites shown in *B*. Bar, 500 nm.

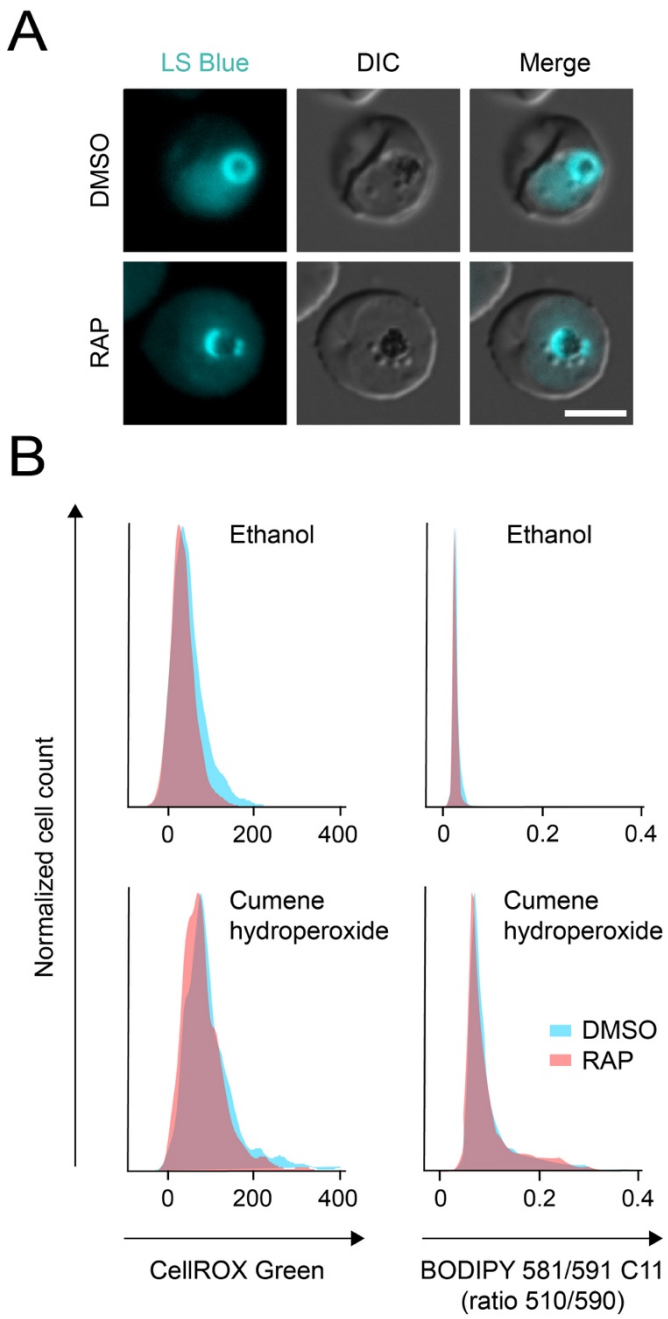

930

931 **Fig. S6.** Absence of *Pf*PV5 does not cause dissipation of the vacuolar pH gradient nor an
932 increase in oxidative stress.

933 (*A*) *Pf*PV5-deficient parasites maintain an intact and acidic food vacuole. Synchronized
934 *pv5::3xHA:*loxP parasites were treated with dimethyl sulfoxide (DMSO) or rapamycin (RAP)
935 from the ring stage onward and were stained with Lysosensor Blue DND-167 (LS Blue) 36
936 hours later. Shown are the LS Blue channel (cyan, left), differential interference contrast
937 images (DIC, centre) and a merge (right). Bar, 5 µm.

938 (*B*) No increased oxidative stress in the absence of *Pf*PV5. Synchronized *pv5::3xHA:loxP*
939 parasites were treated with DMSO or RAP from the ring stage onward, stained with the

940 oxidative stress sensor CellROX Green (left) or with the ratiometric lipid peroxidation dye
941 BODIPY 581/591 C11 (right) 36 hours later and analysed by flow cytometry. In addition,
942 parasites had been treated with the oxidative stress-inducing agent cumene hydroperoxide
943 (bottom) or with ethanol as the solvent control (top). Shown are the histograms of CellROX
944 Green fluorescence intensity or of the 510/590 nm fluorescence ratio of BODIPY 581/591 C11.
945 Results are representative of two independent experiments.

946

947 **Movie S1.** Absence of *Pf*PV5 ablates haemozoin movement within the food vacuole of
948 *Plasmodium falciparum*.

949 Shown are differential interference contrast recordings of dimethyl sulfoxide (DMSO, left) and
950 rapamycin-treated (RAP, right) *pv5::3xHA:loxP* parasites 36 hours following invasion. The
951 video contains 120 frames shown at a 4x acceleration. Elapsed time is indicated in the upper
952 right corner. Bar, 5 µm.

953 **Table S1. Haemozoin crystal morphometry.**

	WT	***pv5-3xHA:loxP***		WT *vs.* DMSO	WT *vs.* RAP	DMSO *vs.* RAP
		DMSO	**RAP**			
Area (μm^2)	0.164 (±0.088)	0.107 (±0.052)	0.102 (±0.039)	***	***	n.s.
Aspect ratio	3.673 (±1.047)	2.781 (±1.061)	1.604 (±0.337)	***	***	***
Branching (%)	0	27.5	96.1			

954 n.s., non-significant; ***, P<0.001; One-way ANOVA and Tukey's multiple comparison test.
955 N>300 crystals.

956 **Table S2. Primer sequences.**

Primer Name	Primer Sequence (restriction sites)	WT (bp)[a]	INT (bp)[b]	EX (bp)[c]	Use[d]	Target	Reference
NT-PbPV5-F-*BamH*I	agttttggatccaaaatgaaattttatagcatttttgcaattg	707			TV	NT Pb*PV5*	This study
NT-PbPV5-R-*Sac*II	agtattccgcggtttaaataacatttctgatttttttctcc				TV	NT Pb*PV5*	This study
5'-PbPTEX88-F-*BamH*I	aaatatggatcctttttttgtgaaataagttgtttggtg	1,496			TV	5' Pb*PTEX88*	This study
5'-PbPTEX88-R-*BamH*I	atatatggatccaattttggggatttcaatctttttaag				TV	5' Pb*PTEX88*	This study
5'-PbHSP101-F-*BamH*I	ttaaaaggatccaaaaattatacaatgcgtgtggc	1,489			TV	5' Pb*HSP101*	This study
5'-PbHSP101-R-*BamH*I	ttttcaggatccatttatagtaaatatagatataattttatcttcattc				TV	5' Pb*HSP101*	This study
T7	taatacgactcactataggg		1,206		GT	T7	-
5'-PbPV5-F	gtgggtcgttatttgtatttttttaatattagg	1,440			GT	5' Pb*PV5*	This study
CT-PbPV5-R1	gatggatcataaccagcaacg				GT	CT Pb*PV5*	This study
5'-PbPTEX88-F	agtacgaagatataatttgaaaagcc		1,091		GT	5' Pb*PTEX88*	This study
5'-PbHSP101-F	tgcaactacattttattacgccc		1,177		GT	5' Pb*HSP101*	This study
CT-PbPV5-F	taaacccgttgatgaaaacactactgttg	261			qPCR	CT Pb*PV5*	This study
CT-PbPV5-R2	ggatcataaccagcaacgtaaagagc				qPCR	CT Pb*PV5*	This study
Pb18S-F	aagcattaaataaagcgaatacatccttac	134			qPCR	Pb*18S-rRNA*	(64)
Pb18S-R	ggagattggttttgacgtttatgtg				qPCR	Pb*18S-rRNA*	(64)
NT-PfPV5-F	attgattgttattatcatttccag	24			gRNA	NT Pf*PV5*	This study
NT-PfPV5-R1	aaacctggaaatgataataacaat				gRNA	NT Pf*PV5*	This study
5'-PfPV5-F	aatgcgggggaggagaaccc	836	730	2,006 / 1,260	GT	5' Pf*PV5*	This study
NT-PfPV5-R2	acaactccatcctatcaaaattaaag				GT	NT Pf*PV5*	This study
CT-PfPV5-F	catgatcattatgtctaaatatagaacc	670			GT	CT Pf*PV5*	This study
3'-PfPV5-R	atgtgaaaaaacttacaaactatataccc		561	2,006 / 1,260	GT	3' Pf*PV5*	This study
LoxP-F	taacttcgtatagcatacattatacg				GT	*loxP*	This study
LoxP-R	aacttcgtataatgtatgctatacg				GT	*loxP*	This study

957 [a] Sizes of Wild-type-specific PCR products.

958 [b] Sizes of integration-specific PCR products.

959 [c] Sizes of excision-diagnostic PCR products (non-excised / excised).

960 [d] Primers used for construction of Transfection Vectors (TV), for GenoTyping (GT), or quantitative real-time PCR -
961 (qPCR). Used primer combinations are indicated in Figures 3*A* and *SI Appendix*, Figures S1*A* and S3*A*.